



Dynamic mode-I delamination in composite DCB under impact loads with tunable dynamic effect

Tianyu Chen^{a,*}, Christopher M. Harvey^{b,c}, Kun Zhang^{a,d,**}, Simon Wang^{b,c}, Vadim V. Silberschmidt^e, Bingchen Wei^{a,d,f,***}

^a Key Laboratory of Microgravity (National Microgravity Laboratory), Institute of Mechanics, Chinese Academy of Sciences, Beijing, 100190, China

^b Department of Aeronautical and Automotive Engineering, Loughborough University, Loughborough Leicestershire, LE11 3TU, UK

^c School of Mechanical and Equipment Engineering, Hebei University of Engineering, Handan, 056038, China

^d School of Engineering Science, University of Chinese Academy of Sciences, Beijing, 100049, China

^e Wolfson School of Mechanical, Electrical and Manufacturing Engineering, Loughborough University, Loughborough Leicestershire, LE11 3TU, UK

^f Center for Materials Science and Optoelectronics Engineering, University of Chinese Academy of Sciences, Beijing, 100049, China

ARTICLE INFO

Keywords:

Double cantilever beam test
Dynamic mode-I energy Release rate
Drop weight impact
Vibration
CFRP

ABSTRACT

A dynamic mode-I energy release rate (ERR) of a double cantilever beam (DCB) under impact from a striker is derived for the first time for isotropic and orthotropic composite materials, accounting for DCB properties, a striker mass and an initial impact velocity. This is achieved in the context of structural vibration analysis by employing beam dynamics. It is found that the initial impact velocity determines the magnitude of the ERR, which is proportional to the velocity squared, while the delamination length ratio and the mass ratio between the striker and the DCB defines the time response. To understand the transient effect, a dynamic factor is defined as a function of the mass ratio. This factor decreases with an increasing striker mass, indicating a transition in the dynamic response from flexural-wave dominant to quasi-static-motion dominant, allowing an tunable dynamic effect. The developed theory is verified against the finite-element simulations for isotropic and orthotropic materials as well as experimental verification using published data. This work allows the measurements of fracture toughness under the impact load with the derived analytical solution. In addition, the developed theory can guide a design of impact tests and provide a fundamental understanding of impact-induced fracture for carbon-fiber-reinforced plastics.

1. Introduction

Carbon-fiber-reinforced-plastics (CFRPs) are a type of laminated composite material, which are of particular interest for light-weight structures in aerospace, automotive, energy, civil engineering and other fields, thanks to their high specific stiffness and strength. One of the main challenges in application of CFRPs is the prevention of delamination or debonding which is seen as one of the most detrimental damages [1].

Delamination, or, in general, interfacial fracture, is generally mixed-mode since delamination tends to be confined to the weak interface

between laminae [2]. Conventionally, however, the fracture behavior of laminated composites is studied with pure-fracture-mode coupon configurations, such as double-cantilever beam (DCB) tests for mode-I fracture [3,4] and end-loaded split (ELS) [5,6] and end-notched flexure (ENF) [7,8] tests for mode-II fracture. Such coupon tests provide measurements of fracture toughness for respective fracture modes. Real-life engineering problems with mixed-mode delamination are therefore solved by considering the decomposition of a total energy release rate (ERR) into its pure-fracture-mode components together with suitable mixed-mode failure criteria [9].

For mode-I delamination with DCB tests in the quasi-static load regime, standard test methods with analytical descriptions are well

* Corresponding author.

** Corresponding author. Key Laboratory of Microgravity (National Microgravity Laboratory), Institute of Mechanics, Chinese Academy of Sciences, Beijing, 100190, China.

*** Corresponding author. Key Laboratory of Microgravity (National Microgravity Laboratory), Institute of Mechanics, Chinese Academy of Sciences, Beijing, 100190, China.

E-mail addresses: chentianyu@imech.ac.cn (T. Chen), zhangkun@imech.ac.cn (K. Zhang), weibc@imech.ac.cn (B. Wei).

| Nomenclature | | | |
|------------------------|--|------------------------------|--|
| A_n | Area of cross-section of beam section n | δ_{ij} | Kronecker delta |
| a | Delamination length | η | Delamination length ratio |
| a_{eff} | Effective delamination length | $\Lambda_i(\eta, \xi)$ | i th mode contribution to total ERR from beam section ② |
| b | Width of beam | λ_i | i th mode eigenvalue |
| E | Young's modulus | ν | Poisson's ratio |
| E^* | Effective Young's modulus | ξ | Mass ratio of total DCB system and striker |
| f_{dyn} | Total dynamic factor | ρ | Density |
| f_{dyn}^1 | Dynamic factor of first vibration mode | $\varphi_{ni}(x)$ | i th mode shape of beam section n |
| G | Total ERR | $\Psi_i(\eta, \xi)$ | i th mode contribution to total ERR from beam section ③ |
| G_{dyn} | ERR component due to total dynamic effect | ω_i | Angular frequency of i th vibration mode |
| G_{st}^U | Quasi-static ERR | <i>Differential notation</i> | |
| h | Thickness of one DCB arm | $w^{(n)}$ | n th partial derivative of w with respect to coordinate x |
| I_n | Second moment of area of beam cross-section for beam section n | | $w^{(n)} = \partial^n w / \partial x^n$ |
| L | Uncracked region length | \dot{w} | first partial derivative of w with respect to time $\dot{w} = \partial w / \partial t$ |
| M | Mass of striker | \ddot{w} | second partial derivative of w with respect to time $\ddot{w} = \partial^2 w / \partial t^2$ |
| $M_n(x, t)$ | Internal bending moment of beam section n | <i>Abbreviations</i> | |
| m | Total mass of the DCB system | CFRP | Carbon fiber reinforced plastic |
| $T_i(t), \dot{T}_i(t)$ | Modal displacement and velocity of i th normal mode | DCB | Double cantilever beam |
| t | Time | ELS | End-loaded split |
| v | Initial impact velocity | ENF | End-notched flexure |
| $w_n(x, t)$ | Deflection of beam section n | ERR | Energy release rate |
| $W_{ni}(x)$ | i th normal mode for beam section n | FEM | Finite-element method |
| α_i | i th mode wavenumber for beam section ① | SHPB | split Hopkinson pressure bar |
| β_i | i th mode wavenumber for beam sections ② and ③ | VCCT | Virtual crack closure technique |

established in standards such as for CFRPs (ASTM D5528 [10] and ISO 15024 [11]) and for adhesives (ISO 25217 [12]). For the dynamic load regime with high loading rates, however, the literature mainly focuses on experimental aspects of high loading rates using a servo-hydraulic machine [13], a drop weight impact [14,15], or a split Hopkinson pressure bar [16,17]. As pointed out in a review [18], a limited upper bound of the loading rate of servo-hydraulic machines make them unsuitable to study the rate-dependent fracture behavior of CFRPs, and, therefore, the SHPB and the drop weight impact are more suitable techniques to study the impact-induced delamination and assess the rate-dependence of fracture toughness. In the mechanical perspective, notion should be given to essences of these experimental loading conditions, which can mainly be put into two categories: (a) high-loading-rate-displacement loads, for instance SPHB and (b) momentum loads, that is, drop weight impact. For the DCB under high-loading rate displacement, Smiley and Pipes [19] first associated the rate effect with the crack-tip opening rate \dot{y}_{ct} that is an extrapolation of applied loading rate v at vicinity of crack tip as $\dot{y}_{\text{ct}} = 3v\varepsilon^2 / (2a^2)$, where ε is the arbitrarily small distance from the crack tip and they chose $\varepsilon = 0.25$ mm without further explanation; the determination of the ERR, then, included the contribution of kinetic energy from quasi-static motion of the applied loading rate with $-33\rho hv^2 / 280$. The significance of this investigation acknowledged the crack-tip opening rate is associated but different from the applied opening rate, and a study of rate effects on the fracture toughness must take this into account. Blackman et al. [20] applied a similar technique to further study the dynamic effect of steady-state crack propagation, including a contribution to the DCB arm displacement from the crack propagation speed using $\dot{u} = du/dt + \dot{a}du/da$, as well as a transient effects considering crack propagation acceleration \ddot{a} . However, these two analytical developments only consider the quasi-static motion and did not take into account of effects of structural vibration, which can nevertheless be significant for the slender DCB configuration, giving a smooth ERR. The authors took these effects into account to develop analytical solutions

and successfully captured the oscillatory nature of the ERR with dynamic effect being an intrinsic property of DCB configuration under high-loading rates [21,22] and not alterable. It is also found that the high-loading rate displacement as the quasi-static motion provides a mean value of the ERR; however, it was also demonstrated that under high-loading rate displacement, the dynamic effect increases with applied loading rates and cannot be avoidable, and this poses a drawback to accurately assess the fracture toughness and its rate effect with considerable oscillatory dynamic factor, a reflection of significant opening-and-closing movement. This is also the case for mode-II delamination with forth-to-back movement at crack tip [23,24]. It is then desirable to have a method capable of manipulating the dynamic effect to alleviate or even cancel the significant opening-and-closing movement at crack tip to ensure a constant opening displacement to study the rate effect of fracture toughness. And in this work, it is found that the momentum loads, that is, drop weight impact, can achieve this.

For the DCBs under drop weight impact as momentum loads, to the best authors' knowledge, there is no analytical solution for the ERR, and effects of the mass of striker and configuration of DCB remains unknown, and researchers instead might have to resort to experimental-numerical methods by incorporating the experimentally measured parameters into finite-element-method (FEM) simulations. Experimental-numerical methods [16,17,25] are usually restricted to specific individual cases with limited transferability of their results. This might be one of the reasons that no standard test employing impact was established to measure the dynamic mode-I fracture toughness [18].

As discussed above, an analytical theory of DCBs under drop weight impact loads is highly desirable to study the dynamic fracture behavior in laminated composites. This aim is achieved in this work with novel findings in the tunable dynamic effect by designating mass ratio between drop weight and DCB system. The development of the theory is presented in Section 2, which is then verified with FEM simulations and published experimental data in Section 3, while the conclusions are given in Section 4. Apart from the findings on delamination in DCB

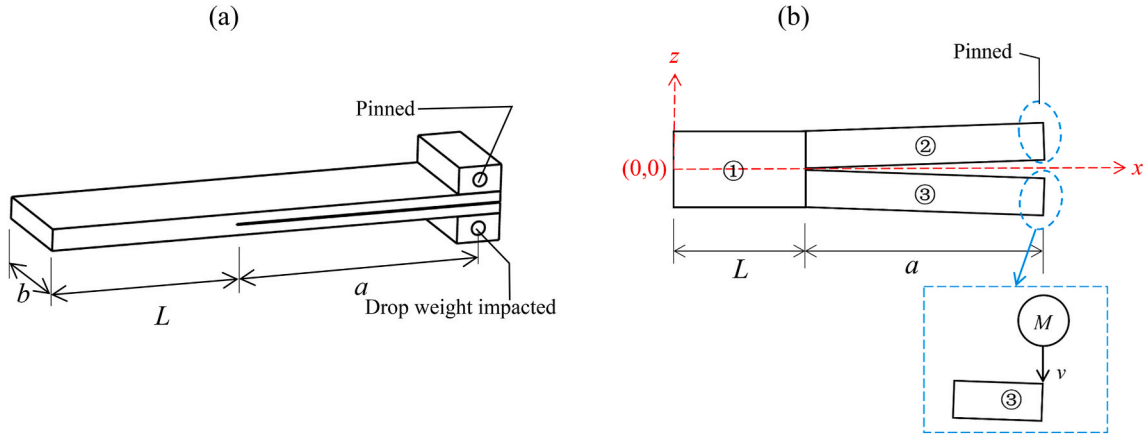


Fig. 1. (a) Schematic of DCB specimen under drop weight impact; (b) boundary condition and coordinate system for three divided beam sections.

under impact loads in this study, the developed analytical techniques can also be applied to analysis of other important aspects of dynamic delamination in CFRPs. A brief roadmap for the next-stage investigations would be as follows: (a) analysis of pure mode-II delamination under impact loads with an emphasis on its difference from that in the mode-I one; (b) investigation of mixed-mode delamination with a focus of the dynamic ERR partition and its difference from the quasi-static partition theories; (c) assessment of the dynamic effect and contribution to it from each vibration mode for impacts with different configurations. All these investigations aim to generate a fundamental and comprehensive understanding of the delamination in CFRPs under impact loads.

2. Theory

In this section, the dynamic mode-I ERR of a DCB specimen under drop weight impact load is derived analytically with consideration of structural vibration by employing beam dynamics. The DCB configuration is shown in Fig. 1(a) with a delamination length of a , an uncracked length of L , a thickness of h for each DCB arm and a width of b . In the drop weight test, the loading block of the upper DCB arm is pinned with an only rotational degree of freedom unconstrained, while the loading block of the lower DCB arm is impacted by a striker. Note that the loading conditions of DCB in Fig. 1(a) is different from that in Ref. [15] where the lower DCB arm was constrained to slide down according to the vertical sliding rail and this might lead to axial force; and when the axial force was significant, as found in Ref. [15] with impact velocity larger than 3 m s^{-1} , the delamination becomes a mixed mode one. However, in Fig. 1(a) the lower DCB arm was not constrained vertically, and no axial force was generated to provide a pure mode-I delamination, and realization of this can be achieved by enlarging the sliding rail in the test configuration in Ref. [15] (a schematic is given in Fig. A.1 in Appendix A).

The full DCB system is modelled as shown in Fig. 1(b) with three beam sections: beam section ① being the uncracked region, beam sections ② and ③ being DCB arms for the delamination region, and their deflections are denoted $w_1(x, t)$, $w_2(x, t)$ and $w_3(x, t)$, respectively. The coordinate was signed with crack tip at $x = L$. The mass of the drop weight is M with initial impact velocity v . Note that other than the boundary conditions and continuity conditions specified in Section 2.1.1, there is no additional constraint to maintain beam section ① horizontally and beam section ① can deflect freely according to the continuity conditions associated with movement of beam sections ② and ③ due to impact. In addition, the simplification and idealization from Fig. 1(a) to Fig. 1(b) neglects the influence of loading blocks assuming their distance from the end of load line longer than 50 mm according to ASTM D5528 [10], or otherwise the corrections should be

made following Annex A.1 in ASTM D5528.

Generally, the ERR of a stationary delamination in DCB under dynamic loading can be determined by crack-tip bending moments by using a crack-tip energy flux integral [22,26,27], and the dynamic ERR for the plane-stress condition is

$$G = \frac{1}{2bE} \left[\frac{M_2^2(L, t)}{I_2} + \frac{M_3^2(L, t)}{I_3} - \frac{M_1^2(L, t)}{I_1} \right], \quad (1)$$

where $M_1(L, t)$, $M_2(L, t)$ and $M_3(L, t)$ are the internal bending moments at crack tip of beam sections ①, ② and ③, respectively; $I_1 = 8bh^3/12$ and $I_2 = I_3 = bh^3/12$ are the corresponding second moment of area of the beam cross-section. Eq. (1) is for assessing the total ERR of the DCB configuration. Further examination of mode-mixity is required, and in light of mode-mixity partition theories [28–30], this is an approximately pure mode-I case (details in Section 2.3 and Appendix F). For the plane-strain condition, the effective Young's modulus of $E^* = E/(1 - \nu^2)$ should replace Young's modulus E in Eq. (1) and throughout this paper. Note that Lagrange's notation $w^{(n)} = \partial^n w / \partial x^n$ is used to denote n th partial derivative of w with respect to the x coordinate, and Newton's dot notation $\dot{w} = \partial w / \partial t$ and $\ddot{w} = \partial^2 w / \partial t^2$ are the first and second partial derivative with respect to time. The deflections of the respective beam sections are derived in Section 2.1.

2.1. Dynamic transverse response of DCB arm

2.1.1. Boundary conditions and assumptions

The boundary condition for beam section ① is free at $x = 0$ allowing the uncracked region deflecting downwards. The boundary condition for beam section ② is pinned at $x = L + a$. And for beam section ③ at free edge $x = L + a$ the rotational degree of freedom is unconstrained without introducing axial force. These conventional boundary conditions are detailed in Appendix B.

The other boundary condition for beam section ③ due to the drop weight impact is given in Eq. (2), following the method proposed in Ref. [31] assuming that the contact between the DCB arm's end and striker is "hard" without elastic contact deformation and shear force at the contact point must be equal to the reversed effective force of the striker.

$$EI_3 w_3^{(3)}(L + a, t) = M \ddot{w}_3(L + a, t). \quad (2)$$

Eq. (2) applies while the striker drives the DCB system downwards without separating from free edge of beam section ③. The maximum ERR is achieved when the striker arrives the maximum displacement after which the DCB arm rebounds and drives the striker back (Fig. H.1).

It is also assumed that $h \ll a$ and $h \ll L$, where the shear is considered to be insignificant, and so the Euler-Bernoulli beam theory applies, and

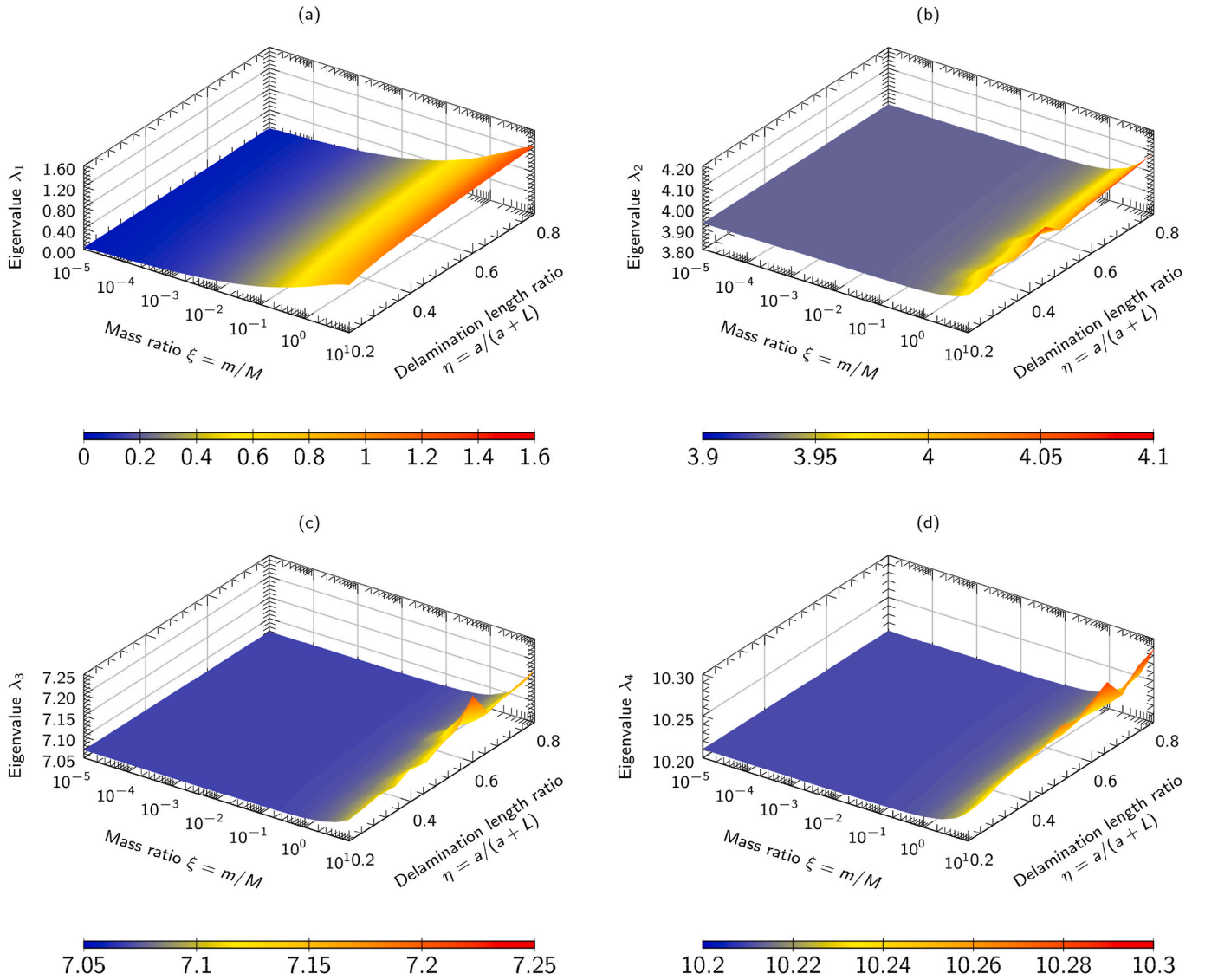


Fig. 2. Eigenvalues for (a) first, (b) second, (c) third and (d) fourth vibration modes.

then the equations of motion for beam sections ①, ② and ③ are

$$EI_1 w_1^{(4)}(x, t) + \rho A_1 \ddot{w}_1(x, t) = 0, \quad (3)$$

$$EI_2 w_2^{(4)}(x, t) + \rho A_2 \ddot{w}_2(x, t) = 0, \quad (4)$$

$$EI_3 w_3^{(4)}(x, t) + \rho A_3 \ddot{w}_3(x, t) = 0, \quad (5)$$

where $A_1 = 2bh$ and $A_2 = A_3 = bh$ are respective areas of the cross-section.

The general solutions for Eqs. (3)–(5) by separation of variables are

$$w_1(x, t) = \sum_{i=1}^{\infty} W_{1i}(x) T_i(t), \quad (6)$$

$$w_2(x, t) = \sum_{i=1}^{\infty} W_{2i}(x) T_i(t), \quad (7)$$

$$w_3(x, t) = \sum_{i=1}^{\infty} W_{3i}(x) T_i(t), \quad (8)$$

where $W_{1i}(x)$, $W_{2i}(x)$ and $W_{3i}(x)$ are the respective i th normal modes; and $T_i(t)$ is the i th modal displacement. Combining Eqs. (3) and (6), (4)

and (7), (5) and (8), three ordinary governing equations for normal modes of respective beam sections and one ordinary equation for modal displacement are derived:

$$W_{1i}^{(4)}(x) - \alpha_i^4 W_{1i}(x) = 0, \quad (9)$$

$$W_{2i}^{(4)}(x) - \beta_i^4 W_{2i}(x) = 0, \quad (10)$$

$$W_{3i}^{(4)}(x) - \beta_i^4 W_{3i}(x) = 0, \quad (11)$$

$$\ddot{T}_i(t) + \omega_i^2 T_i(t) = 0, \quad (12)$$

where α_i and β_i are the wavenumbers with $\alpha_i^4 = \omega_i^2 \rho A_1 / (EI_1)$ and $\beta_i^4 = \omega_i^2 \rho A_2 / (EI_2)$, and ω_i is the angular natural frequency. The solutions for the normal modes and the modal displacement are derived in Sections 2.1.2 to 2.1.3, respectively.

2.1.2. Solutions for normal modes and frequency equation

The normal mode solutions for beam sections ①, ② and ③ in Eqs. (9)–(11) together with the boundary conditions in Tables. B.1, B.2 and B.3 are

$$W_{1i}(x) = C_{1i} \varphi_{1i}(x), \quad (13)$$

$$W_{2i}(x) = C_{i1}\varphi_{2i}(x), \tag{14}$$

$$W_{3i}(x) = C_{i1}\varphi_{3i}(x), \tag{15}$$

where $\varphi_{1i}(x)$, $\varphi_{2i}(x)$ and $\varphi_{3i}(x)$ are corresponding mode shapes:

$$\varphi_{1i}(x) = \cosh(\alpha_i x) + \cos(\alpha_i x) + \frac{C_{i2}}{C_{i1}} [\sinh(\alpha_i x) + \sin(\alpha_i x)], \tag{16}$$

$$\varphi_{2i}(x) = \frac{C_{i3}}{C_{i1}} \sinh[\beta_i(x-L-a)] + \frac{C_{i4}}{C_{i1}} \sin[\beta_i(x-L-a)], \tag{17}$$

$$\begin{aligned} \varphi_{3i}(x) = & \frac{C_{i5}}{C_{i1}} \{ \cosh[\beta_i(x-L-a)] + \cos[\beta_i(x-L-a)] \} \\ & + \frac{C_{i6}}{C_{i1}} \sinh[\beta_i(x-L-a)] + \frac{C_{i7}}{C_{i1}} \sin[\beta_i(x-L-a)], \end{aligned} \tag{18}$$

with C_{i1} , C_{i2} , C_{i3} , C_{i4} , C_{i5} , C_{i6} and C_{i7} being the coefficients to be determined by the orthogonality and continuity conditions.

Particularly, the other boundary condition for normal mode of beam section ③ $W_{3i}(x)$ can be obtained by Eq. (2). Combining Eqs. (8), (11) and (12), this boundary conditions for $W_{3i}(x)$ is then

$$EI_3 W_{3i}^{(3)}(L+a) + \omega_i^2 M W_{3i}(L+a) = 0. \tag{19}$$

Substituting $\omega_i^2 = \beta_i^4 EI_3 / (\rho A_3)$ and Eqs. (15) and (18) into (19), and introducing the delamination length ratio $\eta = a/(a+L)$ and the mass ratio $\xi = m/M$ between the DCB and the striker, where $m = 2\rho b h(L+a)$ is the total mass of the whole DCB system, the relation for coefficients C_{i5} , C_{i6} and C_{i7} is

$$4\beta_i a C_{i5} + \eta \xi C_{i6} - \eta \xi C_{i7} = 0. \tag{20}$$

Now applying the continuity conditions for beam sections ①, ② and ③ at crack tip $x = L$ (Table. B.4) and combining Eq. (20), the following linear equation system for coefficients C_{i1} to C_{i7} is obtained:

$$\begin{aligned} & \begin{bmatrix} \left[\cosh \left[\frac{(1-\eta)\lambda_i}{\sqrt{2\eta}} \right] + \cos \left[\frac{(1-\eta)\lambda_i}{\sqrt{2\eta}} \right] \right] & \left[\sinh \left[\frac{(1-\eta)\lambda_i}{\sqrt{2\eta}} \right] + \sin \left[\frac{(1-\eta)\lambda_i}{\sqrt{2\eta}} \right] \right] & \sinh(\lambda_i) & \sinh(\lambda_i) & 0 & 0 & 0 \\ 0 & 0 & \sinh(\lambda_i) & \sin(\lambda_i) & \cosh(\lambda_i) + \cos(\lambda_i) & -\sinh(\lambda_i) & -\sin(\lambda_i) \\ \left[\sinh \left[\frac{(1-\eta)\lambda_i}{\sqrt{2\eta}} \right] - \sin \left[\frac{(1-\eta)\lambda_i}{\sqrt{2\eta}} \right] \right] & \left[\cosh \left[\frac{(1-\eta)\lambda_i}{\sqrt{2\eta}} \right] + \cos \left[\frac{(1-\eta)\lambda_i}{\sqrt{2\eta}} \right] \right] & -\sqrt{2}\cosh(\lambda_i) - \sqrt{2}\cos(\lambda_i) & 0 & 0 & 0 & 0 \\ 0 & 0 & \cosh(\lambda_i) & \cos(\lambda_i) & \sinh(\lambda_i) - \sin(\lambda_i) & -\cosh(\lambda_i) - \cos(\lambda_i) & \\ 4 \left[\cosh \left[\frac{(1-\eta)\lambda_i}{\sqrt{2\eta}} \right] - \cos \left[\frac{(1-\eta)\lambda_i}{\sqrt{2\eta}} \right] \right] & 4 \left[\sinh \left[\frac{(1-\eta)\lambda_i}{\sqrt{2\eta}} \right] - \sin \left[\frac{(1-\eta)\lambda_i}{\sqrt{2\eta}} \right] \right] & \sinh(\lambda_i) & -\sin(\lambda_i) & -\cosh(\lambda_i) + \cos(\lambda_i) & \sinh(\lambda_i) & -\sin(\lambda_i) \\ 2\sqrt{2} \left[\sinh \left[\frac{(1-\eta)\lambda_i}{\sqrt{2\eta}} \right] + \sin \left[\frac{(1-\eta)\lambda_i}{\sqrt{2\eta}} \right] \right] & 2\sqrt{2} \left[\cosh \left[\frac{(1-\eta)\lambda_i}{\sqrt{2\eta}} \right] - \cos \left[\frac{(1-\eta)\lambda_i}{\sqrt{2\eta}} \right] \right] & -\cosh(\lambda_i) & \cos(\lambda_i) & \sinh(\lambda_i) + \sin(\lambda_i) & -\cosh(\lambda_i) & \cos(\lambda_i) \\ 0 & 0 & 0 & 0 & 4\lambda_i & \eta \xi & -\eta \xi \end{bmatrix} \begin{pmatrix} C_{i1} \\ C_{i2} \\ C_{i3} \\ C_{i4} \\ C_{i5} \\ C_{i6} \\ C_{i7} \end{pmatrix} \\ & = \begin{pmatrix} 0 \\ 0 \\ 0 \\ 0 \\ 0 \\ 0 \\ 0 \end{pmatrix}, \end{aligned} \tag{21}$$

where $\lambda_i = \beta_i a$ is the eigenvalue. For coefficients C_{i1} to C_{i7} to have non-zero solutions, the determinant of coefficient matrix of Eq. (21) must be zero, giving the frequency equations whose solutions are the eigenvalues

as functions of the delamination length ratio η and mass ratio ξ between the DCB system and the striker. The eigenvalues for first four vibration modes are shown in Fig. 2.

Note that eigenvalues λ_i for the DCB system, with the given boundary conditions and configuration, as a function of delamination length ratio η and mass ratio ξ determine the intrinsic dynamic response of the DCB system, such as natural frequency via $\omega_i = (\lambda_i/a)^2 \sqrt{EI_2/(\rho A_2)}$, wave-number via $\beta_i = \lambda_i/a$ and mode shape via Eqs. (16)–(18).

Turning back to the solution of coefficients C_{i1} to C_{i7} , C_{i1} can be obtained by orthogonality condition Eq. (C.5) (derivation in Appendix C) with $i = j$, giving

$$C_{i1}^2 = \frac{1}{(L+a)} \frac{1}{\chi_i}, \tag{22}$$

with

$$\begin{aligned} \chi_i = & \int_0^L [\varphi_{1i}(x)]^2 dx + \frac{1}{2} \int_L^{L+a} [\varphi_{2i}(x)]^2 dx + \frac{1}{2} \int_L^{L+a} [\varphi_{3i}(x)]^2 dx \\ & + \frac{(L+a)}{\xi} [\varphi_{3i}(L+a)]^2. \end{aligned} \tag{23}$$

Then ratios between coefficients, that is, C_{i2}/C_{i1} to C_{i7}/C_{i1} (Appendix D) can be applied to determine each coefficient.

2.1.3. Solution for modal displacement

The general solution for the modal displacement in Eq. (12) is

$$T_i(t) = T_i(0)\cos(\omega_i t) + \frac{\dot{T}_i(0)}{\omega_i} \sin(\omega_i t), \tag{24}$$

where $T_i(0)$ and $\dot{T}_i(0)$ are the initial modal displacement and velocity, respectively. Initially at $t = 0$, the DCB system with beam sections ①, ② and ③ is at its undeformed state, and so, according to Eqs. (6)–(8), $w_1(x, 0) = \sum_{i=1}^{\infty} W_{1i}(x)T_i(0) = 0$, $w_2(x, 0) = \sum_{i=1}^{\infty} W_{2i}(x)T_i(0) = 0$ and $w_3(x, 0)$

$$= \sum_{i=1}^{\infty} W_{3i}(x)T_i(0) = 0, \text{ giving } T_i(0) = 0.$$

For the initial modal velocity, the initial velocity of respective beam sections of the DCB system are $\dot{w}_1(x, 0) = \sum_{i=1}^{\infty} W_{1i}(x)\dot{T}_i(0) = 0$, $\dot{w}_2(x, 0)$

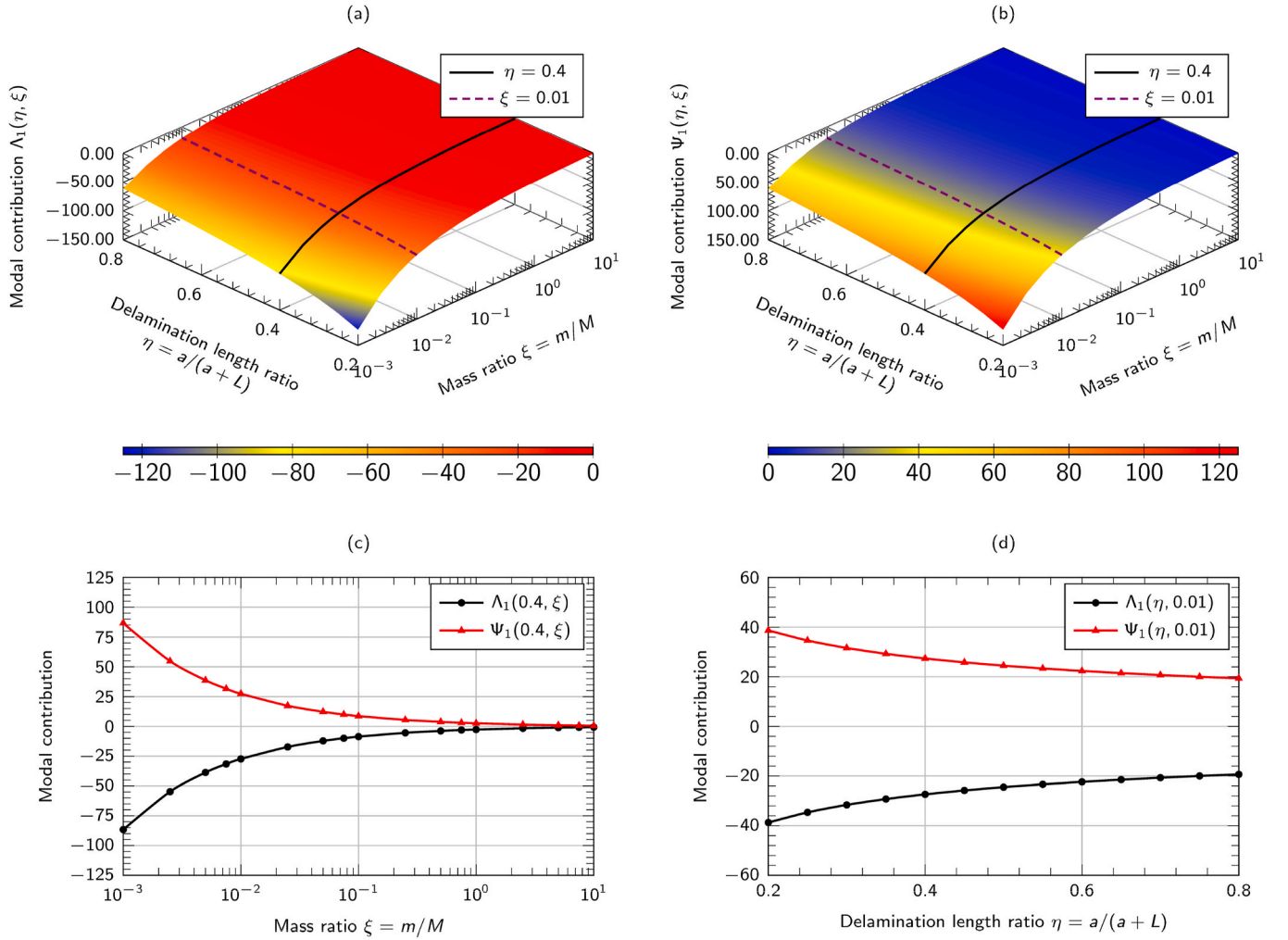


Fig. 3. Effect of mass ratio and delamination length ratio on contribution of first vibration mode to ERR for (a) upper beam and (b) lower beam, (c) comparison for $\eta = 0.4$ and (d) comparison for $\xi = 0.01$.

$= \sum_{i=1}^{\infty} W_{2i}(x)\dot{T}_i(0) = 0$, and $\dot{w}_3(x, 0) = \sum_{i=1}^{\infty} W_{3i}(x)\dot{T}_i(0) = 0$, but the initial velocity at the impact point is $\dot{w}_3(L+a, 0) = \sum_{i=1}^{\infty} W_{3i}(L+a)\dot{T}_i(0) = -v$. Multiplying $\dot{w}_1(x, 0)$ by $W_{1j}(x)$ and integrating over the beam length $(0, L)$, multiplying $\dot{w}_2(x, 0)$ by $W_{2j}(x)/2$ and integrating over the beam length $(L, L+a)$, multiplying $\dot{w}_3(x, 0)$ by $W_{3j}(x)/2$ over the beam length $(L, L+a)$, and, then, summing these integrals together with $(L+a)\dot{w}_3(L+a, 0)W_{3j}(L+a)/\xi$ and applying the orthogonality condition (Eq. (C.5)), the initial modal velocity is found to be

$$\begin{aligned} \dot{T}_i(0) &= \left[\int_0^L \dot{w}_1(x, 0)W_{1i}(x)dx + \frac{1}{2} \int_L^{L+a} \dot{w}_2(x, 0)W_{2i}(x)dx \right. \\ &\quad \left. + \frac{1}{2} \int_L^{L+a} \dot{w}_3(x, 0)W_{3i}(x)dx + \frac{(L+a)}{\xi} \dot{w}_3(L+a, 0)W_{3i}(L+a) \right] \\ &= -v \frac{(L+a)}{\xi} W_{3i}(L+a). \end{aligned} \tag{25}$$

Now, combining the results from Sections 2.1.1 to 2.1.3, the deflections of the beam sections ①, ② and ③ are respectively

$$w_1(x, t) = -v \frac{1}{\xi} \sum_{i=1}^{\infty} \frac{1}{\chi_i \omega_i} \varphi_{3i}(L+a) \varphi_{1i}(x) \sin(\omega_i t), \tag{26}$$

$$w_2(x, t) = -v \frac{1}{\xi} \sum_{i=1}^{\infty} \frac{1}{\chi_i \omega_i} \varphi_{3i}(L+a) \varphi_{2i}(x) \sin(\omega_i t), \tag{27}$$

$$w_3(x, t) = -v \frac{1}{\xi} \sum_{i=1}^{\infty} \frac{1}{\chi_i \omega_i} \varphi_{3i}(L+a) \varphi_{3i}(x) \sin(\omega_i t). \tag{28}$$

2.2. Energy release rate

By combining Eqs. (1) and (26)–(28) with the continuity condition for bending moment at crack tip $EI_1 w_1^{(2)}(L, t) = EI_2 w_2^{(2)}(L, t) + EI_3 w_3^{(2)}(L, t)$ (Table B.4), the total dynamic ERR of the DCB specimen under impact, shown in Fig. 1, is obtained as

$$G = \frac{\rho A_2 v^2}{16b} \left\{ 7 \left[\sum_{i=1}^{\infty} \Lambda_i(\eta, \xi) \sin(\omega_i t) \right]^2 + 7 \left[\sum_{i=1}^{\infty} \Psi_i(\eta, \xi) \sin(\omega_i t) \right]^2 \right. \\ \left. - 2 \left[\sum_{i=1}^{\infty} \Lambda_i(\eta, \xi) \sin(\omega_i t) \right] \left[\sum_{i=1}^{\infty} \Psi_i(\eta, \xi) \sin(\omega_i t) \right] \right\}, \tag{29}$$

where $\Lambda_i(\eta, \xi)$ and $\Psi_i(\eta, \xi)$ are i th mode contribution from beam sections ② and ③ respectively:

$$\Lambda_i(\eta, \xi) = \frac{2}{\xi} \frac{1}{\chi_i} \left[-\frac{C_{i3}}{C_{i1}} \sinh(\lambda_i) + \frac{C_{i4}}{C_{i1}} \sin(\lambda_i) \right] \frac{C_{i5}}{C_{i1}}, \tag{30}$$

$$\Psi_i(\eta, \xi) = \frac{2}{\xi} \frac{1}{\chi_i} \left\{ \frac{C_{i5}}{C_{i1}} [\cosh(\lambda_i) - \cos(\lambda_i)] - \frac{C_{i6}}{C_{i1}} \sinh(\lambda_i) + \frac{C_{i7}}{C_{i1}} \sin(\lambda_i) \right\} \frac{C_{i5}}{C_{i1}}. \tag{31}$$

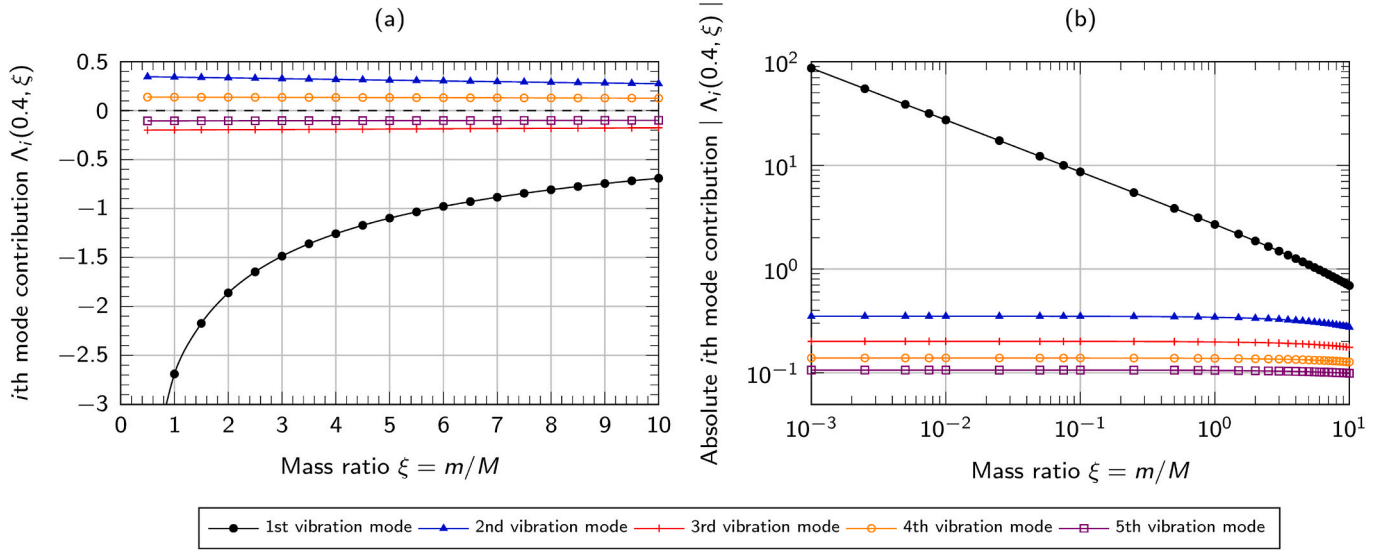


Fig. 4. (a) Effect of mass ratio on contribution of i th vibration mode to ERR with $\eta = 0.4$ and (b) absolute values of contribution.

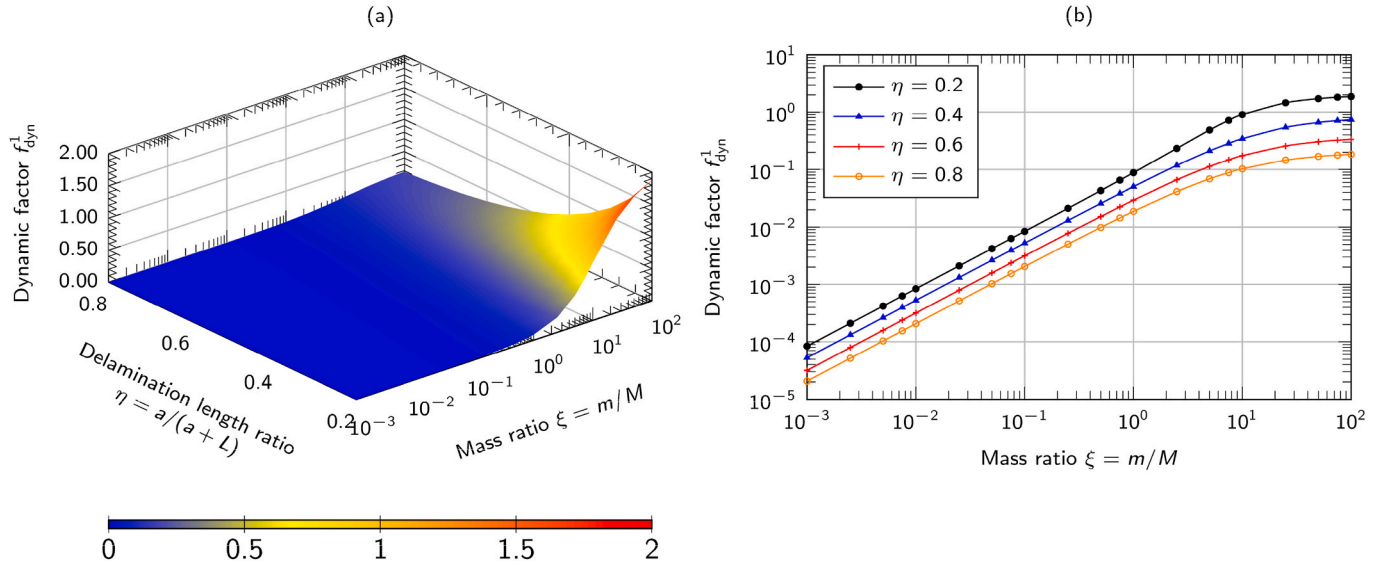


Fig. 5. (a) Effect of mass ratio and delamination length ratio on dynamic factor of first vibration mode and (b) dynamic factor of first vibration mode for typical delamination length ratios.

Note that the parameter $\Lambda_i(\eta, \xi)$ and $\Psi_i(\eta, \xi)$ are dimensionless and only a function of the delamination length ratio η and mass ratio ξ . The contributions of the i th vibration mode to the total ERR from the two DCB arms at the crack region, which $\Lambda_i(\eta, \xi)$ and $\Psi_i(\eta, \xi)$ represent, are therefore universal for DCBs under impact.

It is also worth noting that the impact velocity only determines the magnitude of the total ERR, which is proportional to v^2 , while the delamination length ratio η and the mass ratio ξ defines the time response of dynamic ERR via $\Lambda_i(\eta, \xi)$ and $\Psi_i(\eta, \xi)$, showing a potential attributable contribution to the total ERR.

In the experimental regard of measuring the delamination initiation toughness employing Eq. (29), it is required that the time for delamination initiation be recorded, such as by high-speed cameras and strain gauges.

2.3. Contribution of i th vibration mode to ERR

In Eq. (29), the contribution of the i th vibration mode to the total

ERR is determined by the parameters $\Lambda_i(\eta, \xi)$ and $\Psi_i(\eta, \xi)$. For the first vibration mode, $\Lambda_1(\eta, \xi)$ and $\Psi_1(\eta, \xi)$ are solved and plotted in Fig. 3(a) and (b); particularly, for $\eta = 0.4$, the values of $\Lambda_1(0.4, \xi)$ and $\Psi_1(0.4, \xi)$ are plotted in Fig. 3(c) with respect to various mass ratio ξ (exact values in Table E.1); and for $\xi = 0.01$, their values are plotted in Fig. 3(d) (exact values in Table E.2).

It is seen that $\Lambda_1(\eta, \xi) \approx -\Psi_1(\eta, \xi)$, and note that $\Lambda_1(\eta, \xi)$ and $\Psi_1(\eta, \xi)$, representing the bending moments of first vibration mode at crack tip, are contributions from beam sections ② and ③, respectively, and $\Lambda_1(\eta, \xi) \approx -\Psi_1(\eta, \xi)$, then, indicating a pure mode-I fracture mode from the first vibration mode, according to partition theories [28–30] and experimental support [32]. Note that despite the uncertainty around mode mixity for asymmetric DCBs, i.e., DCB arms with different thickness, the literature is generally in agreement for symmetric DCBs, i.e., DCB arms with same thickness, the case in this study. An examination using William’s partition theory is given in Appendix F. This is also the case for other vibration modes, and detailed comparison are given in Figs. E.1, E.2 and E.3 for the second, third and fourth vibration modes.

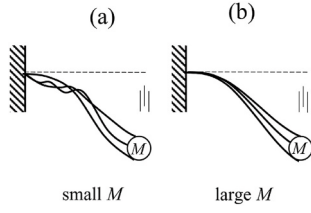


Fig. 6. Beam deflections under impact with a striker with small (a) and large (b) masses.

Table 1
Eigenvalues and modal contribution for $\eta = 0.4$ and $\xi = 0.0255$.

| Mode number | 1 | 2 | 3 | 4 |
|--------------------------|-----------|---------|----------|----------|
| $\lambda_i(0.4, 0.0255)$ | 0.29558 | 3.92691 | 7.06876 | 10.21030 |
| $\Lambda_i(0.4, 0.0255)$ | -17.14258 | 0.35006 | -0.20025 | 0.13847 |

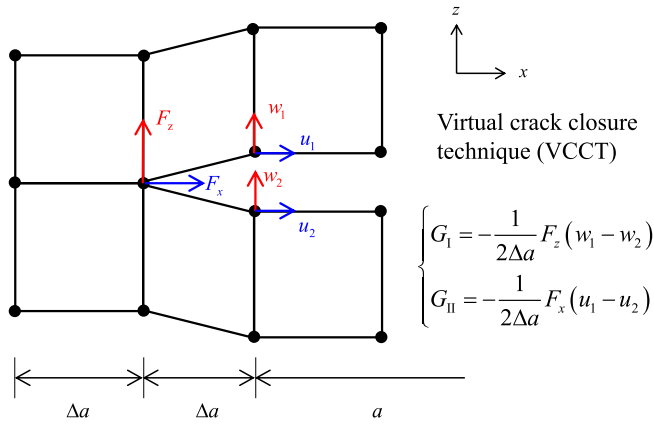


Fig. 7. VCCT for numerical determination of mode-I and -II ERR.

Therefore, the ERR can be simplified by substituting $\Lambda_i(\eta, \xi)$ for $-\Psi_i(\eta, \xi)$ into Eq. (29), giving

$$G = \frac{\rho A_2 v^2}{b} \left[\sum_{i=1}^{\infty} \Lambda_i(\eta, \xi) \sin(\omega_i t) \right]^2. \quad (32)$$

Now the modal contribution from each vibration mode can be studied by investigating the values of $\Lambda_i(\eta, \xi)$ from each vibration modes. For $\eta = 0.4$ (recommended in ASTM D5528), $\Lambda_i(0.4, \xi)$ for the first four vibration modes are plotted in Fig. 4(a) with their absolute values in Fig. 4(b).

It is seen that in Fig. 4, the first vibration mode makes the greatest contribution compared with other vibration modes, and its contribution becomes even significant when the mass ratio ξ is small. The variation of $\Lambda_i(\eta, \xi)$ with the mass ratio ξ provides a very important feature of the time response of the dynamic ERR: (1) when the striker mass is large (and, hence, ξ is small), the first vibration dominates the ERR time response and forms a baseline, around which the contributions of other vibration modes oscillate; (2) when the striker mass is small (ξ is large), the contributions from all vibration modes are comparable, and the total ERR behaves as a coupled noise, without less dominant feature.

2.4. Dynamic factor

To study the dynamic effect associated with the delamination length ratio η and impact mass ratio ξ , a dynamic factor is defined as follows, considering the quasi-static solution. The quasi-static ERR (the super-

script U denotes the strain energy, and the subscript st denotes the quasi-static motion) can be determined in terms of the opening displacement $w_3(L+a, t)$ of the DCB system, as G_{st}^U .

$$G_{st}^U = \frac{9EI_2}{ba^4} \left[\frac{1}{2} w_3(L+a, t) \right]^2 = \frac{\rho A_2 v^2}{b} \left[\sum_{i=1}^{\infty} X_i(\eta, \xi) \sin(\omega_i t) \right]^2, \quad (33)$$

where

$$X_i(\eta, \xi) = \frac{6}{\xi} \frac{1}{\lambda_i} \frac{1}{\lambda_i^2} \left(\frac{C_{i5}}{C_{i1}} \right)^2, \quad (34)$$

where the coefficient ratio C_{i5}/C_{i1} is given in Eq. (D.1). The ERR component due to the dynamic effect is therefore $G_{dyn} = G - G_{st}^U$, and the dynamic factor is defined as

$$f_{dyn} = \frac{G_{dyn}}{G_{st}^U} = \frac{\left[\sum_{i=1}^{\infty} \Lambda_i \sin(\omega_i t) \right]^2}{\left[\sum_{i=1}^{\infty} X_i \sin(\omega_i t) \right]^2} - 1. \quad (35)$$

According to Fig. 4, the dominant vibration mode is the first. It may therefore be insightful to study the dynamic factor with only the first vibration mode, which is

$$f_{dyn}^1 = \frac{[\Lambda_1(\eta, \xi) \sin(\omega_1 t)]^2}{[X_1(\eta, \xi) \sin(\omega_1 t)]^2} - 1 = \frac{\Lambda_1^2(\eta, \xi)}{X_1^2(\eta, \xi)} - 1. \quad (36)$$

For delamination length ratio $0.2 \leq \eta \leq 0.8$ and $0.001 \leq \xi \leq 100$, the dynamic factor f_{dyn}^1 is plotted in Fig. 5(a), and the evolution of f_{dyn}^1 with typical delamination length ratios ($\eta = 0.2, 0.4, 0.6, 0.8$) are plotted with Fig. 5(b) as a function of mass ratio ξ .

As seen in Fig. 5(a) and (b) when $\xi \leq 1$ the first vibration mode dynamic factor f_{dyn}^1 varies log-linearly with respect to the mass ratio ξ , and, therefore, for $\xi \rightarrow 0$ (i.e., a very large striker mass), the dynamic factor approaches to zero $f_{dyn}^1 \rightarrow 0$; when $\xi \geq 1$, the dynamic factor f_{dyn}^1 increases with respect to the mass ratio ξ and tends asymptotically to about 2.02 for $\eta = 0.2$, 0.83 for $\eta = 0.4$, 0.37 for $\eta = 0.6$ and 0.20 for $\eta = 0.8$ (Fig. 5(b)).

This is an interesting observation as one might intuitively consider the opposite: dynamic factor should increase with increasing impact mass, but it is not the case. Considering the eigenvalue solutions in Section 2.1.2 for Fig. 2(a), when the striker mass increases as $\xi \rightarrow 0$, the eigenvalue of the first vibration mode approaches zero, that is, $\lambda_1 \rightarrow 0$, and, therefore, so does the natural frequency of the first vibration mode since $\omega_1 = (\lambda_1/a)^2 \sqrt{EI_2/(\rho A_2)}$, that is, $\omega_1 \rightarrow 0$. The flexural vibration therefore transitions into the quasi-static motion. This is also seen in the mode shape in Eq. (17): as $\lambda_1 \rightarrow 0$, the wavenumber of the first vibration mode $\beta_1 = \lambda_1/a \rightarrow 0$, and so the wavelength goes to infinity, which corresponds to the quasi-static motion.

A similar phenomenon was also reported in Refs. [33,34]. As illustrated in Fig. 6, as flexural vibration changes to quasi-static motion with $\xi \rightarrow 0$, the ERR component G_{st}^U due to the strain energy of quasi-static motion becomes increasingly close to the total ERR G , with the ERR component G_{dyn} due to the dynamic effect and the dynamic factor both approaching zero.

The significance of this finding is that it demonstrates the dynamic effect can be tunable and adjusted by experimental setup with various focuses of researchers. In addition, for significantly small mass ratio ξ (with large drop weight), the response of the DCB system tends to be same as the quasi-static one, and it might be assumed that the deflections of beam sections hold for various delamination length ratios, by employing Freund's solution [26], the ERR can be related to the delamination propagating speed, giving

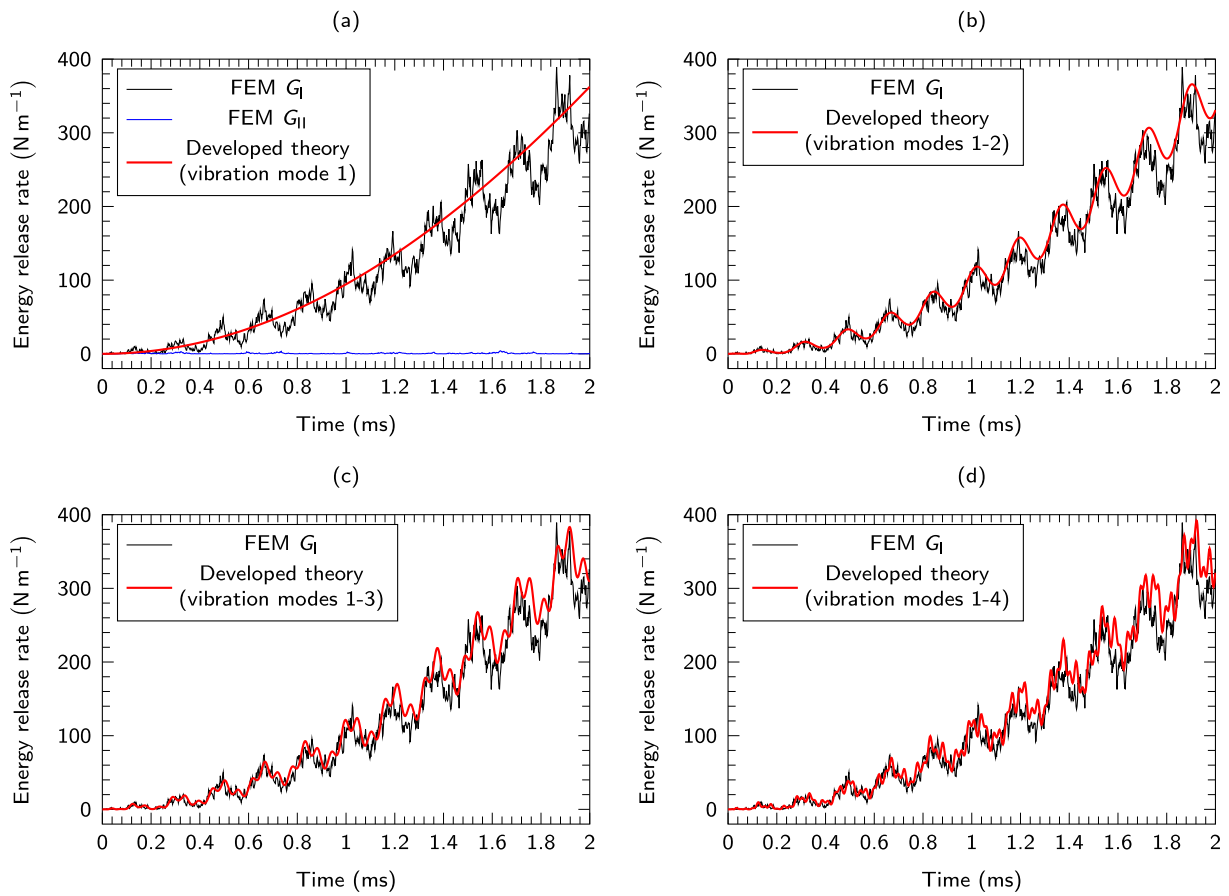


Fig. 8. Comparison of dynamic ERR versus time results obtained with developed theory and FEM with increasing numbers of vibration modes for isotropic material.

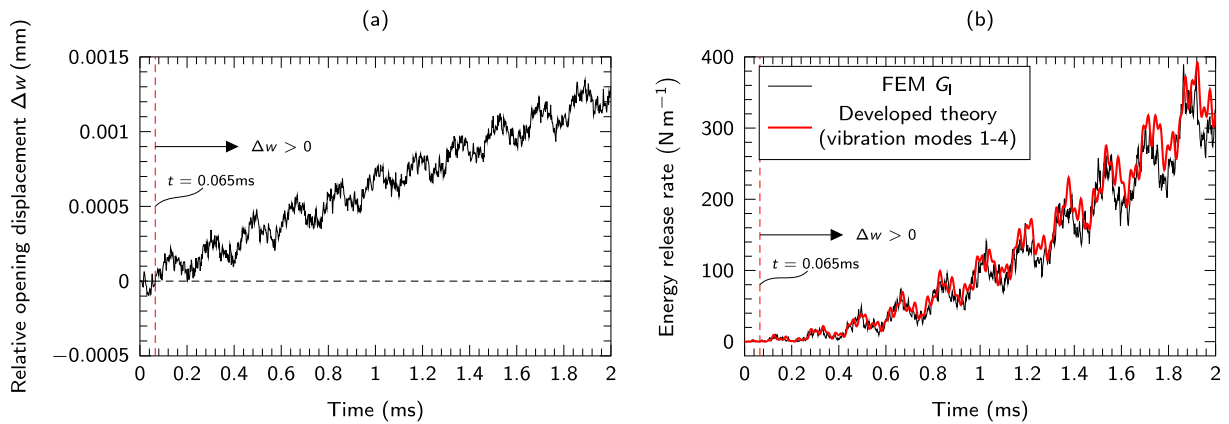


Fig. 9. (a) Relative opening displacement at the vicinity of crack tip; (b) corresponding ERR comparison between developed theory and FEM.

Table 2
Material properties of unidirectional T800H/3900-2 graphite/epoxy composite.

| | | |
|-----------------------|---------------------|---------------------|
| $E_{11} = 154.72$ GPa | $E_{22} = 7.58$ GPa | $E_{33} = 7.58$ GPa |
| $G_{12} = 4.27$ GPa | $G_{13} = 4.27$ GPa | $G_{23} = 2.88$ GPa |
| $\nu_{12} = 0.32$ | $\nu_{13} = 0.32$ | $\nu_{23} = 0.32$ |
| $E_{1f} = 143.13$ GPa | | |

Table 3
Eigenvalues and modal contribution for $\eta = 0.4$ and $\xi = 0.0318$.

| Mode number | 1 | 2 | 3 | 4 |
|--------------------------|-----------|---------|----------|----------|
| $\lambda_i(0.4, 0.0255)$ | 0.31239 | 3.92699 | 7.06881 | 10.21033 |
| $\Lambda_i(0.4, 0.0255)$ | -15.34176 | 0.35001 | -0.20023 | 0.13847 |

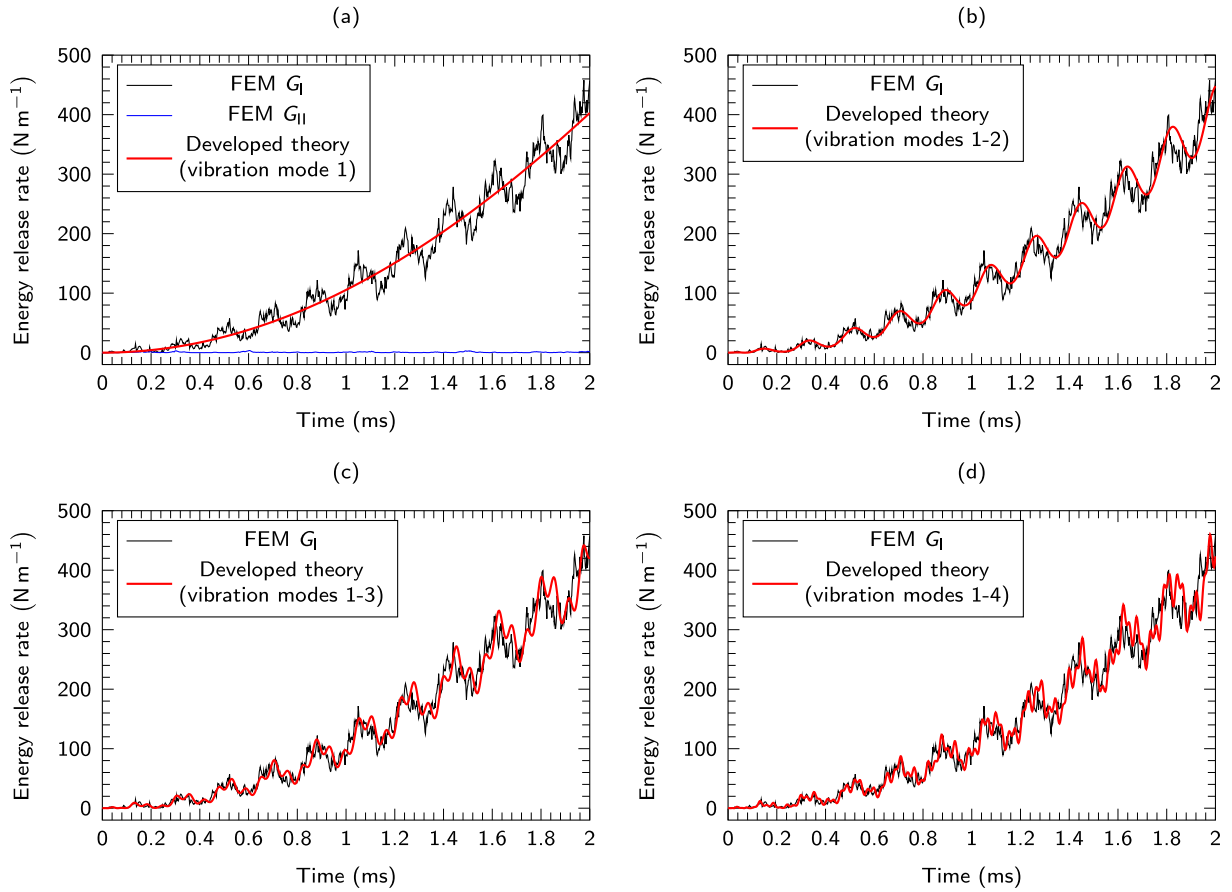


Fig. 10. Comparison of dynamic ERR versus time results obtained with developed theory and FEM with increasing numbers of vibration modes for orthotropic fiber-reinforced composite.

$$G = \frac{\rho A_2 v^2}{b} \left(1 - \frac{\dot{a}^2}{C_0^2}\right) \left[\sum_{i=1}^{\infty} \Lambda_i(\eta, \xi) \sin(\omega_i t) \right]^2 \quad (37)$$

$$= \frac{\rho A_2 v^2}{b} \left(1 - \frac{\dot{a}^2}{C_0^2}\right) \left[\sum_{i=1}^{\infty} X_i(\eta, \xi) \sin(\omega_i t) \right]^2,$$

where \dot{a} is the delamination propagating speed and $C_0 = \sqrt{E/\rho}$ is the longitudinal wave speed.

2.5. Crack-tip compliance correction

The above derivation for the isotropic DCB under an impact load considers the uncracked region as a beam section (beam section ①) without taking account of the effect of interfacial stiffness between the upper and lower DCB arms. Still, shear compliance of the uncracked region due to small interfacial stiffness (for instance, adhesively bonded interface) may be significant and requires correction.

The simplest method for uncracked-region compliance was developed by Kanninen [35] by introducing an elastic Winkler foundation to model the interface between the DCB arms. Subsequently, various models were suggested, such as Pasternak foundation [36], a normal stress distribution [37], a combination of Euler-Bernoulli and Timoshenko beam formations [38], a rotational spring for a crack tip [39] and a Timoshenko beam on elastic foundation [40]; the details and comparison of these modeling techniques can be found in Ref. [41]. Nevertheless, one difficulty of these methods is their complicated analytical solutions that are not easy to obtain and implement. As for direct engineering applications, such as in ASTM D5528 (for CFRPs) and ISO 25217 (for adhesives), an additional delamination length Δ is usually experimentally determined by relating the effective delamination

length $a_{\text{eff}} = (a + \Delta)$ to the cube root of the compliance to compensate for the uncracked-region shear compliance and crack-tip rotation. Particularly, the authors previously developed a relation between the interfacial stiffness based on the elastic Winkler foundation, this effective delamination length a_{eff} and the additional delamination length Δ [42]:

$$\Delta = a_{\text{eff}} - a = \frac{1}{\gamma} \sqrt[4]{\frac{(2a^3\gamma^3 + 6a^2\gamma^2 + 3)^2}{4(a\gamma + 1)^2}} - a, \quad (38)$$

where $\gamma = \sqrt[4]{k/(4EI)}$ and the elastic Winkler foundation stiffness is for an isotropic DCB; $\gamma = \sqrt[4]{k/(4E_{11}I)}$ and $k = E_{33}b/h$ for a composite DCB with E_{11} and E_{33} being the longitudinal and transverse moduli of the orthotropic composite materials. Note that for the isotropic DCB, the foundation stiffness is of the same order as that of the DCB arm and can be deemed as a rigid interface. Also, since the DCB is modelled as three-beam sections, the shear forces from these sections at the crack tip are represented, and the shear effect of the uncracked region might be ignored. Still, this is not the case for orthotropic composite materials, since the foundation stiffness usually is considerably smaller than the longitudinal modulus with significant shear strain at crack tip. So, the shear-compliance correction, for instance using Eq. (38), for the uncracked region must be considered, and this is further verified in Sections 3.2 and 3.3.

3. Numerical and experimental verifications

3.1. Numerical verification for isotropic DCB

FEM simulations were used to verify the analytical theory developed

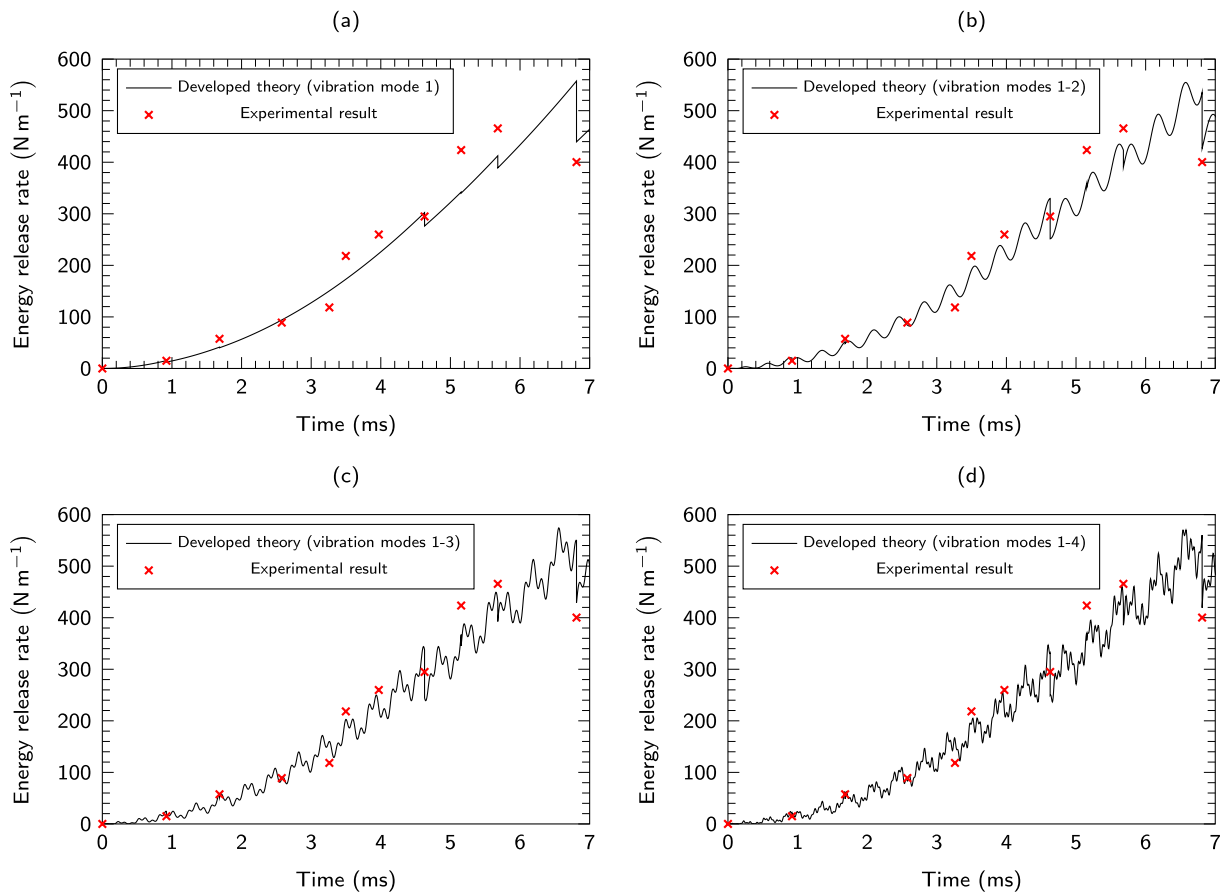


Fig. 11. Comparison of dynamic ERR versus time results obtained with developed theory and experiments with increasing numbers of vibration modes.

in Section 2 for the total dynamic ERR. The geometries for the DCB specimen are as follows: the length of the uncracked region is $L = 75$ mm and the delamination length is $a = 50$ mm (according to ASTM D5528), giving a total length of 125 mm and a delamination length ratio of $\eta = 0.4$; the total thickness $2h = 4$ mm, and the width $b = 1$ mm. Isotropic elastic properties were used with the Young's modulus of 100 GPa, the Poisson's ratio of 0.3, and density of 10^3 kg m $^{-3}$. The impactor mass is 0.0196 kg (giving a mass ratio $\xi = 0.0255$), and the initial impact velocity is 2 m s $^{-1}$. For the given delamination length ratio $\eta = 0.4$ and mass ratio $\xi = 0.0255$, the eigenvalues λ_i and modal contribution to ERR Λ_i are shown in Table 1.

A 2D FEM model of the full DCB was built in Abaqus/Explicit using four-node plane-stress elements (CPS4R) in SI (mm) consistent units, and the uniform element size was 0.05 after convergence study. The uncracked region was modelled by sharing nodes of two DCB arms. The impact took place at the upper surface of the lower beam at the free end (Appendix G). The total dynamic ERR from the FEM was calculated using the virtual crack closure technique (VCCT) [43] as shown in Fig. 7 and compared to that obtained with the analytical theory.

Fig. 8 shows a comparison of the mode-I dynamic ERR from the analytical theory developed in Section 2 (red line) and from FEM simulation results (black line) with various numbers of vibration modes (long-term ERR comparison in Appendix H). In Fig. 8(a), note that for the FEM results the mode-II ERR is also examined which has a maximum value of 3.5 N m $^{-1}$ (blue line) and is insignificant compared to mode-I ERR. Therefore, the DCB under impact from a striker can be seen as a pure mode-I fracture case, consistent with the findings in Section 2.3. It is seen that the first vibration mode provides an "average" value of the ERR (Fig. 8(a)). By adding more vibration modes, the total ERR begins to oscillate around the ERR component from the first vibration mode, and becomes increasingly close to the FEM simulation results. The developed

analytical theory and FEM simulations are generally in excellent agreement, for a sufficient number of vibration modes.

Also note that the analytical theory does not take into account the contact or interpenetration, but at the beginning of the impact there can be interpenetration at the vicinity of crack tip, which, nevertheless, alleviates and disappears with the increasing opening displacement. The relative opening displacement at the vicinity of crack tip $\Delta w = w_1 - w_2$ for VCCT (Fig. 7) is checked, and result is in Fig. 9.

It is seen that at the very beginning of the impact up to 0.065 ms, the beam sections ② and ③ can experience interpenetration (Fig. 9(a)). In reality at this period, the ERR should be zero since the opening displacement is restrained; however, the analytical model gives a maximum prediction for ERR of 1.86 N m $^{-1}$ (Fig. 9(b)). Considering the entire ERR time response, the influence of the interpenetration at the beginning of impact can be seen as negligible.

3.2. Numerical verification for orthotropic fiber-reinforced composite

In this section, the developed theory is verified against a simulation of an orthotropic CFRP material. To apply the developed theory, the conventional methods for determining the elastic modulus, as suggested in ASTM D5528, can be used to calculate the dynamic mode-I ERR in Eq. (32) with the longitudinal modulus of elasticity E_{11} or flexural modulus E_{1f} . As indicated in Ref. [44], the results based on E_{11} are less accurate than those with E_{1f} , and, therefore, E_{1f} is employed together with Eq. (32) to determine the ERR.

The orthotropic material properties of unidirectional T800H/3900-2 CFRP, as tabulated in Table 2, were taken from Ref. [45] and adopted for an orthotropic FEM simulation. The same DCB dimensions of Section 3.1 were used.

Note that the transverse modulus E_{33} is far smaller than the longi-

tudinal modulus E_{11} , and shear compliance due to the interfacial stiffness is significant, and correction is required. By employing Eq. (38), for the foundation stiffness of $k = E_{33}b/h = 3.79$ GPa, the additional delamination length to compensate is $\Delta = 3.17$ mm, and, therefore, the effective delamination length $a_{\text{eff}} = 53.17$ mm is used. The density of T800H/3900-2 was taken from manufacturer's data sheet as 1.25×10^3 kg m⁻³, giving a mass ratio of $\xi = 0.0318$. The eigenvalues and modal contribution are given in Table 3.

The comparison between the analytical solutions and the FEM simulation results are shown in Fig. 10 with various vibration modes. As before, the first vibration mode determines the average value of the total ERR; by adding more vibration modes, the magnitude of the developed theory approaches the FEM result. The frequencies predicted with the analytical solution, however, are not as accurate. This may be due to the inaccuracy of the isotropy assumption in modeling the orthotropic composite material analytically. The discrepancy between the analytical solution and the FEM simulation in terms of frequency is not significant, and the analytical solution can still accurately predict the amplitude of the ERR for each vibration mode giving a reasonable assessment of the magnitude of the total ERR.

3.3. Experimental verification

Although the analytical configuration free of axial force to ensure a pure mode-I delamination in this study is different from experimental setup in Ref. [15], it was found that when the loading rate is smaller than 3 m s^{-1} , it is still a pure mode-I case, which can be used to further validate the proposed theory in Section 2. The experimental data for loading rate of 1.5 m s^{-1} and impact mass of 7 kg was used from the reference. Note that the 'interface Young's modulus' as called in Ref. [15] is 2.9 GPa smaller than 'laminate Young's modulus' of 63 GPa, crack-tip compliance has to be considered using Eq. (38).

The comparison between the analytical solutions with various vibration modes and the experimental results are shown in Fig. 11. It is seen that with adding more vibration modes, the ERR derived using the proposed theory becomes increasing close to the experimental results, further verifying the developed theory.

4. Conclusion

The theory of a full DCB under impact from a striker was derived for the first time including the effect of structural vibration, providing analytical solutions for the dynamic deflection and the ERR. The dynamic ERR is a function of the DCB properties, the initial impact velocity and the mass ratio between the DCB arm and the striker. It was found that the dynamic ERR is proportional to the square of the initial impact velocity and the mass ratio determines the dynamic ERR time response. And, therefore, the dynamic effect can be tunable by designating DCB configuration of delamination length ratio and mass ratio between the striker and the DCB.

The dynamic effect was studied by defining a dynamic factor as the contribution to the total ERR from dynamic effects normalized against the ERR for the quasi-static motion. It was found that the first vibration mode made the main contribution to the total dynamic ERR for small mass ratios, and that this dynamic factor decreased with the increasing mass ratio until the response was dominated by quasi-static motion.

The analytical theory was verified against the FEM simulations and experimental results from the literature. Two numerical cases were considered – an isotropic bi-layer composite and a laminated CFRP DCB – and one experimental case of initial impact velocity of 1.5 m s^{-1} were considered. The results from the developed analytical theory are in excellent agreement with the FEM and experimental results.

To the best of the authors' knowledge, the dynamic mode-I ERR of a DCB test under impact with the striker has not been solved before including the effects of structural dynamics and beam vibration. Moreover, previous investigations in the literature ignored the effect of structural vibration, leading to the conclusion that the dynamic effect was not significant in mode-I loading. It was demonstrated in this work, however, that structural vibration did make a significant contribution to the ERR and could not be neglected but adjustable.

The derived theory is applicable in various applications, such as to measure the dynamic mode-I delamination toughness of materials, or to study the impact-induced fracture behavior.

Author contributions

Tianyu Chen: Conceptualization, Methodology, Formal analysis, Writing-Original Draft. **Christopher M. Harvey:** Methodology, Formal analysis, Writing-Review&Editing. **Kun Zhang:** Visualization, Resources, Funding acquisition. **Simon Wang:** Methodology, Visualization, Writing-Review&Editing. **Vadim V. Silberschmidt:** Writing-Review&Editing, Supervision. **Bingchen Wei:** Project administration, Resources, Funding acquisition. All authors have read and agreed to the published version of the manuscript.

Declaration of competing interest

The authors declare that they have no known competing financial interests or personal relationships that could have appeared to influence the work reported in this paper.

Data availability

No data was used for the research described in the article.

Acknowledgement

This work was supported by the National Natural Science Foundation of China (Grant No. 11790292, No. 12272392).

Appendices.

Appendix A. DCB testing configurations

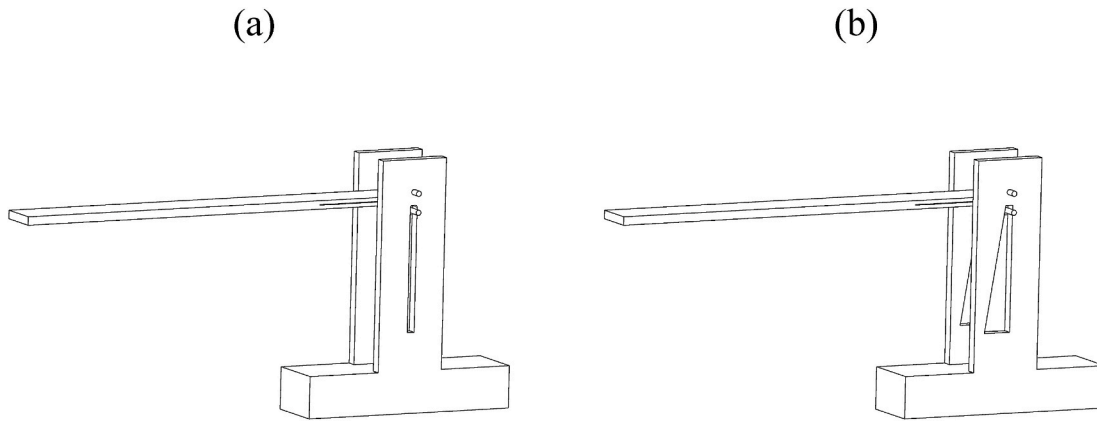


Fig. A.1. Testing configurations: (a) Ref. [15] and (b) proposed in this study

Appendix B. Boundary conditions and continuity conditions

Table. B.1

Boundary conditions for normal mode of beam section ①

| Coordinate | Deflection $w_1(x, t)$ | Normal modes $W_{1i}(x)$ |
|------------|--|--|
| $x = 0$ | $EI_1 w_1^{(2)}(0, t) = 0$ $EI_1 w_1^{(3)}(0, t) = 0$ | $W_{1i}^{(2)}(0) = 0$ $W_{1i}^{(3)}(0) = 0$ |

Table. B.2

Boundary conditions for normal mode of beam section ②

| Coordinate | Deflection $w_2(x, t)$ | Normal modes $W_{2i}(x)$ |
|-------------|---|--|
| $x = L + a$ | $w_2(L + a, t) = 0$ $EI_2 w_2^{(2)}(L + a, t) = 0$ | $W_{2i}(L + a) = 0$ $W_{2i}^{(2)}(L + a) = 0$ |

Table. B.3

Boundary conditions for normal mode of beam section ③

| Coordinate | Deflection $w_3(x, t)$ | Normal modes $W_{3i}(x)$ |
|-------------|--------------------------------|---------------------------|
| $x = L + a$ | $EI_3 w_3^{(2)}(L + a, t) = 0$ | $W_{3i}^{(2)}(L + a) = 0$ |

Table. B.4

Continuity conditions

| | Deflection | Normal modes |
|----------------|--|--|
| Deflection | $w_1(L, t) = w_2(L, t) = w_3(L, t)$ | $W_{1i}(L) = W_{2i}(L) = W_{3i}(L)$ |
| Slope | $w_1^{(1)}(L, t) = w_2^{(1)}(L, t) = w_3^{(1)}(L, t)$ | $W_{1i}^{(1)}(L) = W_{2i}^{(1)}(L) = W_{3i}^{(1)}(L)$ |
| Bending moment | $EI_1 w_1^{(2)}(L, t) = EI_2 w_2^{(2)}(L, t) + EI_3 w_3^{(2)}(L, t)$ | $8W_{1i}^{(2)}(L) = W_{2i}^{(2)}(L) + W_{3i}^{(2)}(L)$ |
| Shear force | $EI_1 w_1^{(3)}(L, t) = EI_2 w_2^{(3)}(L, t) + EI_3 w_3^{(3)}(L, t)$ | $8W_{1i}^{(3)}(L) = W_{2i}^{(3)}(L) + W_{3i}^{(3)}(L)$ |

Appendix C. Derivation of orthogonality condition

Integrating Eq. (9) twice by parts and applying the boundary conditions for $W_{1i}(x)$ in Table. B.1 to have

$$\omega_i^2 \frac{\rho A_1}{EI_1} \int_0^L W_{1i}(x)W_{1j}(x)dx = W_{1j}(L)W_{1i}^{(3)}(L) - W_{1j}^{(1)}(L)W_{1i}^{(2)}(L) + \int_0^L W_{1i}^{(2)}(x)W_{1j}^{(2)}(x)dx. \tag{C.1}$$

Similarly, for beam section ②, integrating Eq. (10) twice by parts with the boundary conditions for $W_{2i}(x)$ in Table B.2, and for beam section ③, integrating Eq. (11) twice by parts with the boundary conditions for $W_{3i}(x)$ in Table B.3

$$\omega_i^2 \frac{\rho A_2}{EI_2} \int_L^{L+a} W_{2i}(x)W_{2j}(x)dx = -W_{2i}^{(3)}(L)W_{2j}(L) + W_{2j}^{(1)}(L)W_{2i}^{(2)}(L) + \int_L^{L+a} W_{2i}^{(2)}(x)W_{2j}^{(2)}(x)dx, \tag{C.2}$$

$$\omega_i^2 \frac{\rho A_3}{EI_3} \int_L^{L+a} W_{3i}(x)W_{3j}(x)dx = \left[\begin{array}{l} -\frac{\omega_i^2}{EI_3} MW_{3i}(L+a)W_{3j}(L+a) \\ -W_{3i}^{(3)}(L)W_{3j}(L) + W_{3j}^{(1)}(L)W_{3i}^{(2)}(L) \end{array} \right] + \int_L^{L+a} W_{3i}^{(2)}(x)W_{3j}^{(2)}(x)dx. \tag{C.3}$$

Then, summing Eqs. (C.1), (C.2) and (C.3) with the continuity conditions in Table B.4, subtracting itself with i and j exchanged, and introducing mass ratio $\xi = m/M$ with $m = 2\rho bh(L+a)$ (the total mass of the DCB system) to have

$$\left(\omega_i^2 - \omega_j^2 \right) \left[\begin{array}{l} \int_0^L W_{1i}(x)W_{1j}(x)dx + \frac{1}{2} \int_L^{L+a} W_{2i}(x)W_{2j}(x)dx \\ + \frac{1}{2} \int_L^{L+a} W_{3i}(x)W_{3j}(x)dx + \frac{(L+a)}{\xi} W_{3i}(L+a)W_{3j}(L+a) \end{array} \right] = 0. \tag{C.4}$$

Note that the natural frequency ω_i is unique, that is, for $i \neq j$, $\omega_i \neq \omega_j$, and, therefore, the terms in bracket in Eq. (C.4) must be zero for $i \neq j$; and incorporating the case for $i = j$, the orthogonality condition is obtained:

$$\int_0^L W_{1i}(x)W_{1j}(x)dx + \frac{1}{2} \int_L^{L+a} W_{2i}(x)W_{2j}(x)dx + \frac{1}{2} \int_L^{L+a} W_{3i}(x)W_{3j}(x)dx + \frac{(L+a)}{\xi} W_{3i}(L+a)W_{3j}(L+a) = \delta_{ij}. \tag{C.5}$$

Appendix D. Coefficient ratios

Employing the continuity conditions in Table B.4 to normal modes in Eqs. (13)–(15), the coefficients C_{i2} , C_{i3} , C_{i4} , C_{i5} , C_{i6} and C_{i7} can be expressed linearly with respect to C_{i1} , and their ratios are

$$\begin{pmatrix} C_{i2}/C_{i1} \\ C_{i3}/C_{i1} \\ C_{i4}/C_{i1} \\ C_{i5}/C_{i1} \\ C_{i6}/C_{i1} \\ C_{i7}/C_{i1} \end{pmatrix} = \begin{pmatrix} \left\{ \sinh \left[\frac{\sqrt{2}}{2} \frac{(1-\eta)}{\eta} \lambda_i \right] + \sin \left[\frac{\sqrt{2}}{2} \frac{(1-\eta)}{\eta} \lambda_i \right] \right\} & \sinh(\lambda_i) & \sin(\lambda_i) & 0 & 0 & 0 \\ 0 & \sinh(\lambda_i) & \sin(\lambda_i) & [\cosh(\lambda_i) + \cos(\lambda_i)] & -\sinh(\lambda_i) & -\sin(\lambda_i) \\ \left[\cosh \left[\frac{\sqrt{2}}{2} \frac{(1-\eta)}{\eta} \lambda_i \right] + \cos \left[\frac{\sqrt{2}}{2} \frac{(1-\eta)}{\eta} \lambda_i \right] \right] & -\sqrt{2} \cosh(\lambda_i) & -\sqrt{2} \cos(\lambda_i) & 0 & 0 & 0 \\ 0 & \cosh(\lambda_i) & \cos(\lambda_i) & [\sinh(\lambda_i) - \sin(\lambda_i)] & -\cosh(\lambda_i) & -\cos(\lambda_i) \\ 4 \left[\sinh \left[\frac{\sqrt{2}}{2} \frac{(1-\eta)}{\eta} \lambda_i \right] - \sin \left[\frac{\sqrt{2}}{2} \frac{(1-\eta)}{\eta} \lambda_i \right] \right] & \sinh(\lambda_i) & -\sin(\lambda_i) & -[\cosh(\lambda_i) - \cos(\lambda_i)] & \sinh(\lambda_i) & -\sin(\lambda_i) \\ 2\sqrt{2} \left[\cosh \left[\frac{\sqrt{2}}{2} \frac{(1-\eta)}{\eta} \lambda_i \right] - \cos \left[\frac{\sqrt{2}}{2} \frac{(1-\eta)}{\eta} \lambda_i \right] \right] & -\cosh(\lambda_i) & \cos(\lambda_i) & [\sinh(\lambda_i) + \sin(\lambda_i)] & -\cosh(\lambda_i) & \cos(\lambda_i) \end{pmatrix}^{-1} \tag{D.1}$$

$$\begin{pmatrix} -\left\{ \cosh \left[\frac{\sqrt{2}}{2} \frac{(1-\eta)}{\eta} \lambda_i \right] + \cos \left[\frac{\sqrt{2}}{2} \frac{(1-\eta)}{\eta} \lambda_i \right] \right\} \\ 0 \\ -\left\{ \sinh \left[\frac{\sqrt{2}}{2} \frac{(1-\eta)}{\eta} \lambda_i \right] - \sin \left[\frac{\sqrt{2}}{2} \frac{(1-\eta)}{\eta} \lambda_i \right] \right\} \\ 0 \\ 4 \left\{ \cosh \left[\frac{\sqrt{2}}{2} \frac{(1-\eta)}{\eta} \lambda_i \right] - \cos \left[\frac{\sqrt{2}}{2} \frac{(1-\eta)}{\eta} \lambda_i \right] \right\} \\ 2\sqrt{2} \sinh \left[\frac{\sqrt{2}}{2} \frac{(1-\eta)}{\eta} \lambda_i \right] + \sin \left[\frac{\sqrt{2}}{2} \frac{(1-\eta)}{\eta} \lambda_i \right] \end{pmatrix}.$$

Appendix E. Modal contributions to ERR

Table E.1

Magnitudes of $\Lambda_1(0.4, \xi)$ and $\Psi_1(0.4, \xi)$ for various mass ratios

| Mass ratio ξ | 0.001 | 0.005 | 0.01 | 0.05 | 0.1 | 0.5 | 1 | 5 | 10 |
|-----------------------|--------|--------|--------|--------|-------|-------|-------|-------|-------|
| $\Lambda_1(0.4, \xi)$ | -86.60 | -38.73 | -27.38 | -12.24 | -8.65 | -3.84 | -2.69 | -1.10 | -0.69 |
| $\Psi_1(0.4, \xi)$ | 86.60 | 38.72 | 27.37 | 12.21 | 8.61 | 3.76 | 2.58 | 0.93 | 0.53 |

Table E.2

Magnitudes of $\Lambda_1(\eta, 0.01)$ and $\Psi_1(\eta, 0.01)$ for various mass ratios

| Delamination length ratio η | 0.2 | 0.3 | 0.4 | 0.5 | 0.6 | 0.7 | 0.8 |
|----------------------------------|--------|--------|--------|--------|--------|--------|--------|
| $\Lambda_1(\eta, 0.01)$ | -38.73 | -31.62 | -27.38 | -24.49 | -22.35 | -20.69 | -19.36 |
| $\Psi_1(\eta, 0.01)$ | 38.70 | 31.60 | 27.37 | 24.48 | 22.35 | 20.69 | 19.36 |

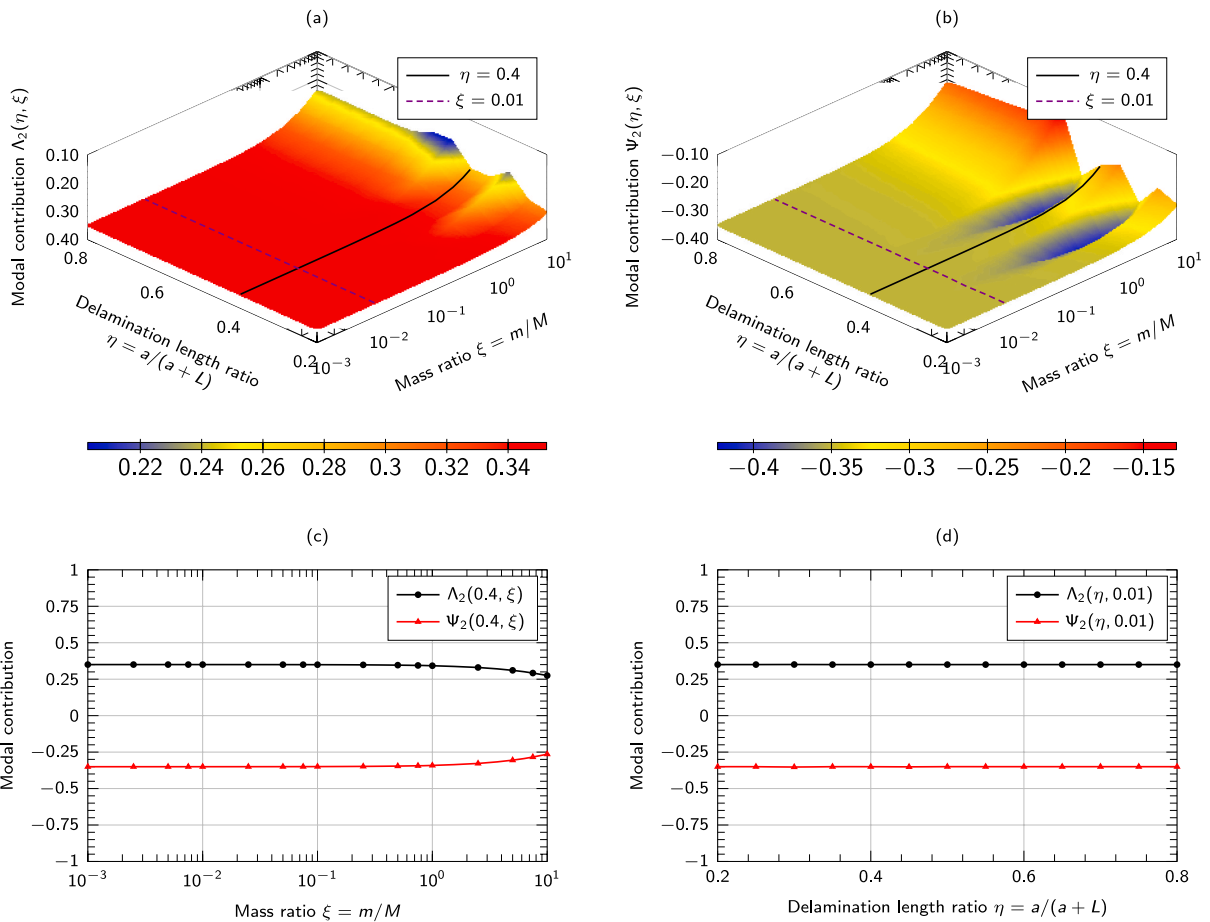


Fig. E.1. Effect of mass ratio and delamination length ratio on contribution of second vibration mode to ERR for (a) upper beam and (b) lower beam, (c) comparison for $\eta = 0.4$ and (d) comparison for $\xi = 0.01$

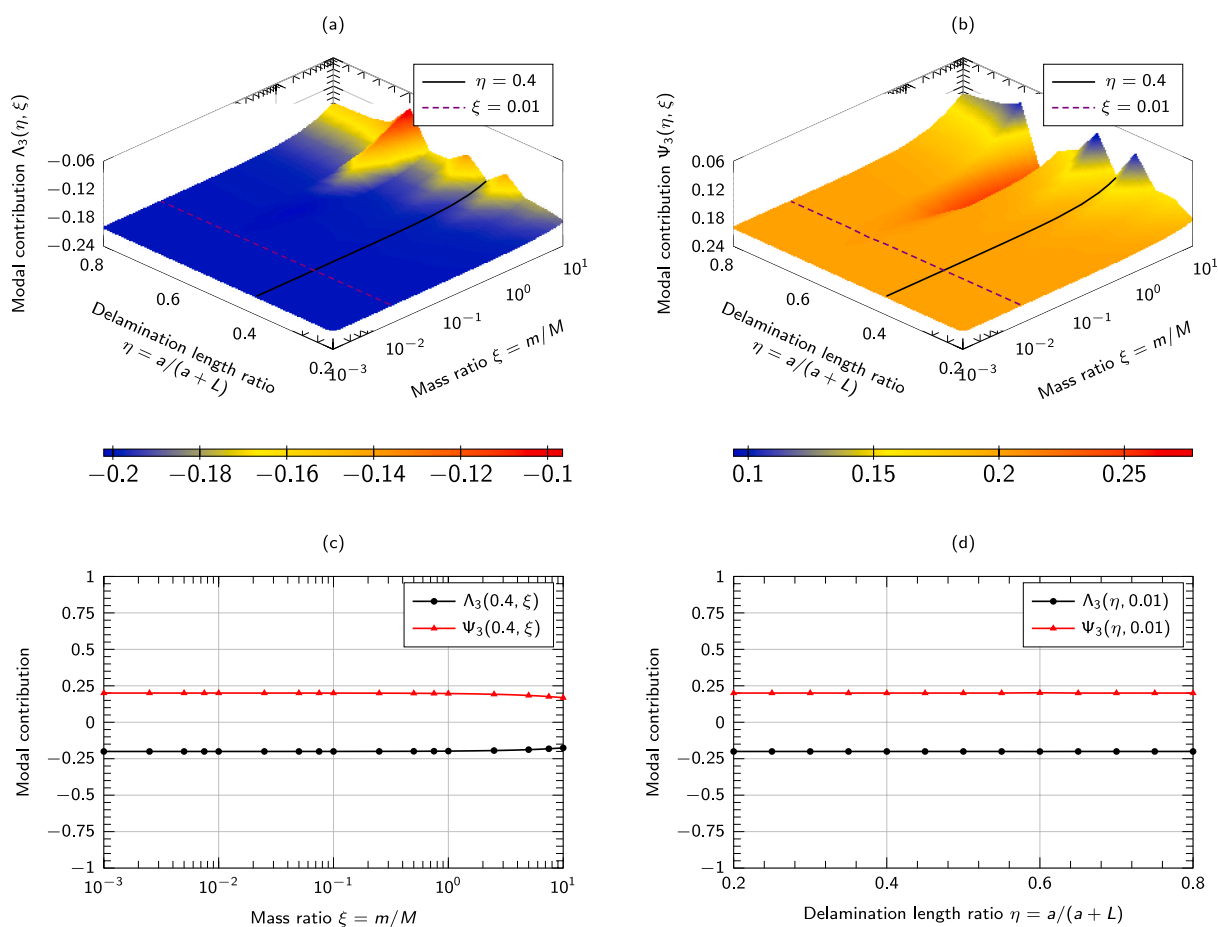


Fig. E.2. Effect of mass ratio and delamination length ratio on contribution of third vibration mode to ERR for (a) upper beam and (b) lower beam, (c) comparison for $\eta = 0.4$ and (d) comparison for $\xi = 0.01$

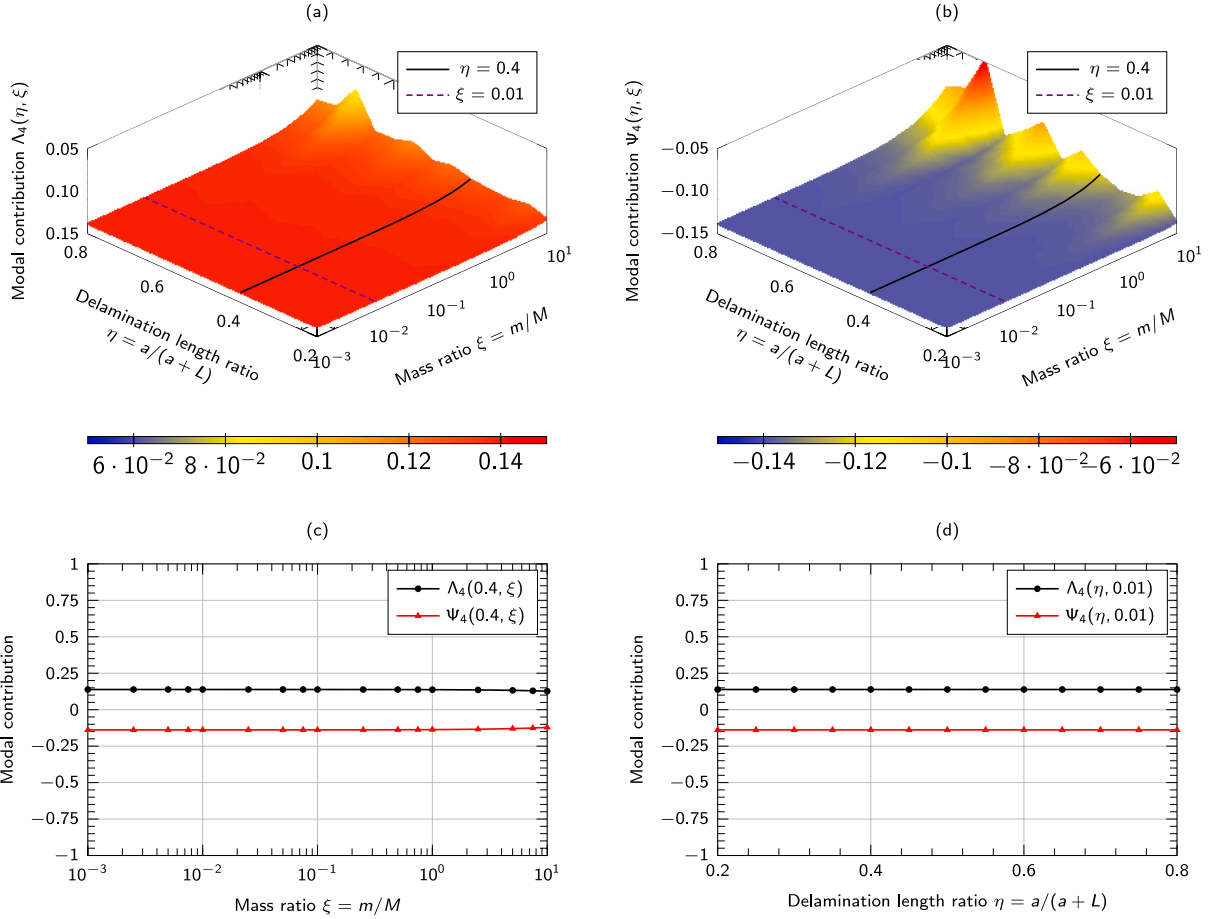


Fig. E.3. Effect of mass ratio and delamination length ratio on contribution of fourth vibration mode to ERR for (a) upper beam and (b) lower beam, (c) comparison for $\eta = 0.4$ and (d) comparison for $\xi = 0.01$

Appendix F. Examination of mode mixity

According to William's partition theory [28], the mode-I and -II ERR are respectively:

$$G_I = \frac{M_I^2}{bEI_1} \frac{(1 + \psi)}{16(1 - \zeta)^3}, \tag{F.1}$$

$$G_{II} = \frac{M_{II}^2}{bEI_1} \frac{3}{16} \frac{(1 - \zeta)}{\zeta^2} (1 + \zeta), \tag{F.2}$$

where $\zeta = h/(2h) = 1/2$ is the thickness ratio, $\psi = (1 - \zeta)^3/\zeta^3$ and M_I and M_{II} are partitioned bending moment pairs given as

$$M_2(L, t) = M_{II} - M_I, \tag{F.3}$$

$$M_3(L, t) = \psi M_{II} + M_I, \tag{F.4}$$

where $M_2(L, t)$ and $M_3(L, t)$ being the bending moments of beam sections ② and ③ at crack tip, respectively.

Note that in Section 2.3, it is found that $\Lambda_i(\eta, \xi) \approx -\psi_i(\eta, \xi)$, which represents the bending moments $M_2(L, t)$ and $M_3(L, t)$ respectively, and therefore, $M_2(L, t) \approx -M_3(L, t)$. By applying this condition to Eqs. (F.3) and (F.4), $M_{II} = 0$ which gives $G_{II} = 0$, demonstrating a pure mode-I case.

Appendix G. FEM model for full DCB

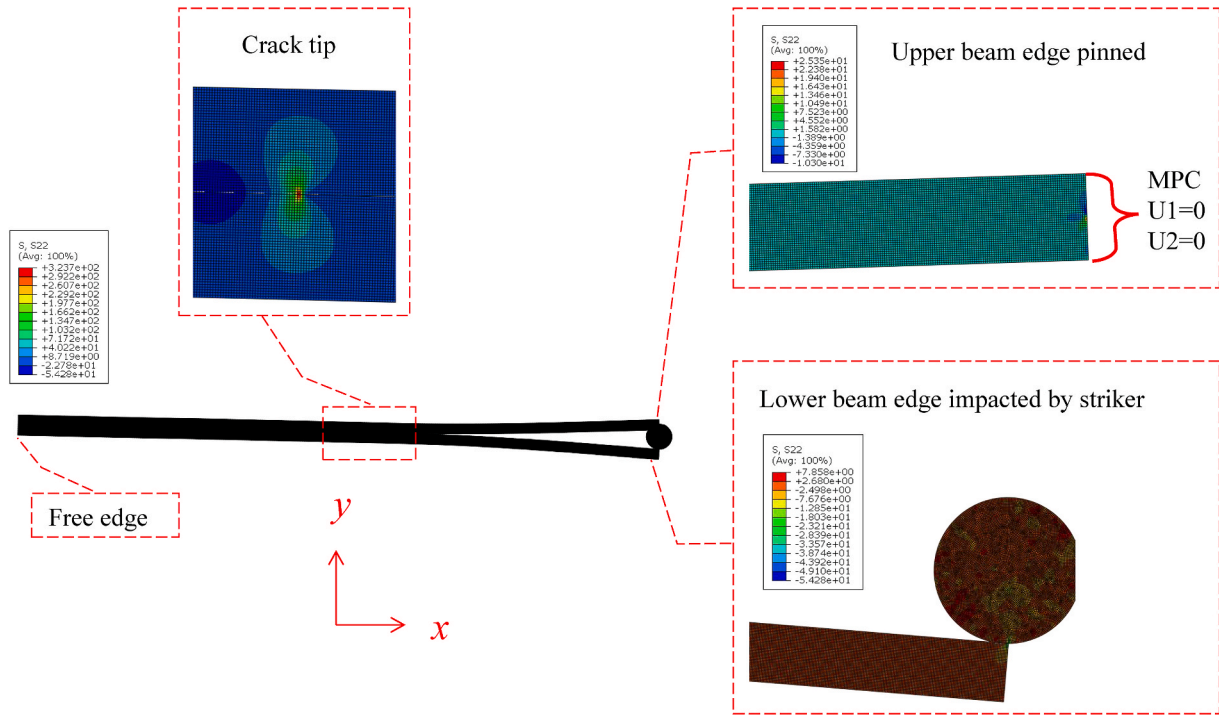


Fig. G.1. Full DCB FEM model

Appendix H. Long-term ERR evolution

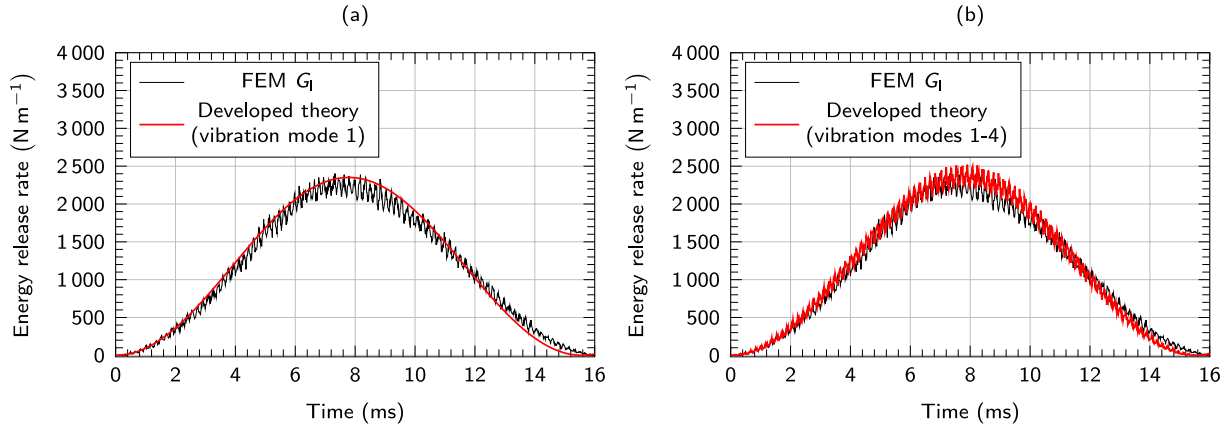


Fig. H.1. Long-term ERR evolution with first (a) and first four vibration modes (b)

References

- [1] M.R. Wisnom, The role of delamination in failure of fibre-reinforced composites, *Philos. Trans. R. Soc. A Math. Phys. Eng. Sci.* 370 (2012) 1850–1870.
- [2] C.M. Harvey, S. Wang, Experimental assessment of mixed-mode partition theories, *Compos. Struct.* 94 (2012) 2057–2067.
- [3] J.C. Ding, W. Xu, Determination of mode I interlaminar fracture toughness of composite by a wedge-insert double cantilever beam and the nonlinear J integral, *Compos. Sci. Technol.* 206 (2021), 108674.
- [4] F. Cepero, I.G. García, J. Justo, V. Mantić, F. París, An experimental study of the translaminar fracture toughnesses in composites for different crack growth directions, parallel and transverse to the fiber direction, *Compos. Sci. Technol.* 181 (2019), 107679.
- [5] B. M'membe, M. Yasaee, S.R. Hallett, I.K. Partridge, Effective use of metallic Z-pins for composites' through-thickness reinforcement, *Compos. Sci. Technol.* 175 (2018) 77–84, 2019.
- [6] D. Quan, F. Bologna, G. Scarselli, A. Ivanković, N. Murphy, Mode-II fracture behaviour of aerospace-grade carbon fibre/epoxy composites interleaved with thermoplastic veils, *Compos. Sci. Technol.* 191 (2020), 108065.
- [7] Z. Li, Z. Wang, W. Lu, X. Zhou, T. Suo, Loading rate dependence of mode II fracture toughness in laminated composites reinforced by carbon nanotube films, *Compos. Sci. Technol.* 215 (2021), 109005.
- [8] M.F.S.F. de Moura, R.D.F. Moreira, F.M.G. Ramírez, Influence of geometric and material parameters on the mode II interlaminar fatigue/fracture characterization of CFRP laminates, *Compos. Sci. Technol.* 210 (2021), 108819.
- [9] J.R. Reeder, An evaluation of mixed-mode delamination failure criteria, *NASA Tech. Memo.* (1992), 104210.

- [10] ASTM D5528, "Standard Test Method for Mode I Interlaminar Fracture Toughness of Unidirectional Fiber-Reinforced Polymer Matrix Composites," ASTM International.
- [11] ISO 15024, "Fibre-Reinforced Plastic Composites - Determination of Mode I Interlaminar Fracture Toughness, GIC, for Unidirectionally Reinforced Materials," International Standard Organization.
- [12] ISO 25217, "Adhesives - Determination of the Mode I Adhesive Fracture Energy of Structural Adhesive Joints Using Double Cantilever Beam and Tapered Double Cantilever Beam Specimens," International Standard Organization.
- [13] G. Hug, P. Thévenet, J. Fitoussi, D. Baptiste, Effect of the loading rate on mode I interlaminar fracture toughness of laminated composites, *Eng. Fract. Mech.* 73 (2006) 2456–2462.
- [14] B.R.K. Blackman, et al., The failure of fibre composites and adhesively bonded fibre composites under high rates of test - Part I Mode I loading-experimental studies, *J. Mater. Sci.* 30 (1995) 5885–5900.
- [15] M. Colin de Verdiere, A.A. Skordos, M. May, A.C. Walton, Influence of loading rate on the delamination response of untufted and tufted carbon epoxy non crimp fabric composites: mode I, *Eng. Fract. Mech.* 96 (2012) 11–25.
- [16] C. Sun, C. Han, A method for testing interlaminar dynamic fracture toughness of polymeric composites, *Compos. B Eng.* 35 (2004) 647–655.
- [17] H. Liu, H. Nie, C. Zhang, Y. Li, Loading rate dependency of Mode I interlaminar fracture toughness for unidirectional composite laminates, *Compos. Sci. Technol.* 167 (2018) 215–223.
- [18] M. May, Measuring the rate-dependent mode I fracture toughness of composites - a review, *Compos. Part A Appl. Sci. Manuf.* 81 (2016) 1–12.
- [19] A.J. Smiley, R.B. Pipes, Rate effects on mode I interlaminar fracture toughness in composite materials, *J. Compos. Mater.* 21 (1987) 670–687.
- [20] B.R.K. Blackman, A.J. Kinloch, Y. Wang, J.G. Williams, The failure of fibre composites and adhesively bonded fibre composites under high rates of test: Part II mode I loading - dynamic effects, *J. Mater. Sci.* 31 (1996) 4451–4466.
- [21] T. Chen, C.M. Harvey, S. Wang, V.V. Silberschmidt, Dynamic interfacial fracture of a double cantilever beam, *Eng. Fract. Mech.* 225 (2020), 106246.
- [22] T. Chen, et al., Assessment of dynamic mode-I delamination driving force in double cantilever beam tests for fiber-reinforced polymer composite and adhesive materials, *Compos. Sci. Technol.* 228 (2022), 109632.
- [23] T. Chen, C.M. Harvey, S. Wang, V. V Silberschmidt, Theory of dynamic mode-II delamination in end-loaded split tests, *Compos. Part C 3* (2020), 100055.
- [24] T. Chen, C.M. Harvey, S. Wang, V.V. Silberschmidt, Theory of dynamic mode-II delamination in end-notched flexure tests, *Compos. Struct.* 274 (2021), 114332.
- [25] C. Guo, C.T. Sun, Dynamic mode-I crack-propagation in a carbon/epoxy composite, *Compos. Sci. Technol.* 58 (1998) 1405–1410.
- [26] L.B. Freund, *Dynamic Fracture Mechanics*, Cambridge University Press, 1990.
- [27] T. Chen, C.M. Harvey, S. Wang, V. V Silberschmidt, Delamination propagation under high loading rate, *Compos. Struct.* 253 (2020), 112734.
- [28] J.G. Williams, On the calculation of energy release rates for cracked laminates, *Int. J. Fract.* 36 (1988) 101–119.
- [29] J.W. Hutchinson, Z. Suo, Mixed mode cracking in layered materials, *Adv. Appl. Mech.* 29 (1991) 63–191.
- [30] C.M. Harvey, S. Wang, Mixed-mode partition theories for one-dimensional delamination in laminated composite beams, *Eng. Fract. Mech.* 96 (2012) 737–759.
- [31] Goldsmith Werner, *Impact*, Edward Arnold LTD., London, 1960.
- [32] C.M. Harvey, M.R. Eplett, S. Wang, Experimental assessment of mixed-mode partition theories for generally laminated composite beams, *Compos. Struct.* 124 (2015) 10–18.
- [33] G.A.O. Davies, R. Olsson, Impact on composite structures, *Aeronaut. J.* 108 (2004) 541–563.
- [34] R. Olsson, Analytical model for delamination growth during small mass impact on plates, *Int. J. Solid Struct.* 47 (2010) 2884–2892.
- [35] M.F. Kanninen, An augmented double cantilever beam model for studying crack propagation and arrest, *Int. J. Fract.* 9 (1973) 83–92.
- [36] J.G. Williams, End corrections for orthotropic DCB specimens, *Compos. Sci. Technol.* 35 (1989) 367–376.
- [37] J.M. Whitney, Stress analysis of the double cantilever beam specimen, *Compos. Sci. Technol.* 23 (1985) 201–219.
- [38] R. Olsson, A simplified improved beam analysis of the DCB specimen, *Compos. Sci. Technol.* 43 (1992) 329–338.
- [39] B. Balendran, On the double cantilever beam specimen for mode-I interface delamination, *J. Appl. Mech. Trans. ASME* 61 (1994) 471–473.
- [40] K. Kondo, Analysis of double cantilever beam specimen, *Adv. Compos. Mater.* 4 (1995) 355–366.
- [41] R. Olsson, On improper foundation models for the DCB specimen, *ICCM Int. Conf. Compos. Mater.* (2007) 1–6.
- [42] T. Chen, C.M. Harvey, S. Wang, V.V. Silberschmidt, Analytical corrections for double-cantilever beam tests, *Int. J. Fract.* 229 (2021) 269–276.
- [43] R. Krueger, Virtual crack closure technique: history, approach, and applications, *Appl. Mech. Rev.* 57 (2004) 109–143.
- [44] ASTM D7905, "Standard Test Method for Determination of the Mode II Interlaminar Fracture Toughness of Unidirectional Fiber-Reinforced Polymer Matrix Composites," ASTM International.
- [45] B.D. Davidson, R.D. Bialaszewski, S.S. Sainath, A non-classical, energy release rate based approach for predicting delamination growth in graphite reinforced laminated polymeric composites, *Compos. Sci. Technol.* 66 (2006) 1479–1496.